UPPSALA
UNIVERSITET

Utrecht University

Self-Assembled Monolayers for Perovskite Solar Cells

Author
Jan P. Cuperus, BSc.

Supervision
dr. B. J. Kim
prof. dr. P. E. de Jongh
dr. G. Boschloo

Gerrit Boschloo Group
Department of Chemistry - Ångström Laboratory
Uppsala Universitet

Nanomaterials Science - Master´s Programme
Utrecht University

Internship Report - July 2020

Abstract

Perovskite solar cells have gone through tremendous improvements the past years. Record efficiencies are approaching those of crystalline Si solar cell technology, but on other aspects many improvements can still be made. For commercialization, its stability is the main point of concern, while from fundamental perspective the issue of hysteresis is highly interesting. With more and more developments being made on the bulk structures, the interfaces are gaining interest, as these are now bottlenecks for further developments.

Here, two different surface modifications have been investigated. Firstly, the surface of SnO_2 was modified using a molecule with a permanent dipole moment in attempt to improve charge extraction from the absorber layer into the electron transport material. Secondly, functionalization of the surface of fluorine-doped tin oxide was attempted using a redox-active species. In this case, the idea was to create a selective contact based on a monolayer of the redox-active molecule. For both molecules, assessment of the presence of the monolayer was proven to be difficult. With respect to control samples, no improvements in solar cell performance have been achieved.

The author can be contacted via LinkedIn or e-mail: j.p.cuperus@students.uu.nl.

Contents

1 Introduction

One could write a book, if not multiple, to discuss the need for a dramatic change to the world's energy supply, but here it will be summarized through Fig. 1.1. Ever since the industrial revolution, fossil fuel powered machines allowed mankind to achieve things that its (pre)historical ancestors could have only dreamt of. The same developments however, also stretch the earth in its ability to provide life in the way we know it. This is arguably best reflected in the rise of global temperatures as a result of rising CO_2 levels in the atmosphere. Current policies to counteract the effects of global warming include a shift away from fossil fuel based energy, with a lot of it being replaced by electricity as the energy source. Solar cells, that convert the energy of sunlight into electrical energy, have been predicted to contribute significantly to the energy production of the future [1].

Since the year 2000, the total installed capacity of solar photovoltaic (PV) systems has already increased tremendously, with an increase of 22 % in 2019 alone (see Fig. 1.1b) [3]. The biggest part, ca. 90 %, of all installed solar PV systems are based on crystalline silicon (cSi) modules. cSi has been the world leading material for PV applications since many years, which can partly be ascribed to the development in high purity silicon production processes, driven by the electronics industry. Although lab cell efficiencies of more than 20 % were already achieved before 1990 [4], widespread application of cSi solar cell modules only really took off when economic viability was achieved and PV electrictry prices were comparable to that of other electricity sources [1].

The optical and electronic properties of silicon impose requirements for its use in solar cells and result in the need for high processing temperatures and thick, rigid end products. Therefore, cSi solar cells are not applicable or economical in all situations, for example some forms of integrated PV. From a plethora of different solar cell types that are able to circumvent these problems, perovskite based solar cells have shown to be superior in terms of efficiency. In these solar cells, the thickness of the absorber material is $< 1\,\mu m$, opening possibilities for application on flexible substrates Additionally, the fabrication process usually employs low-temperature, solution-based methods. The field of perovskite solar cells is relatively young, starting in 2009 with a report of cells showing an efficiency of 3.9 % [5]. Since then, the field has developed at a staggering pace and the record for cell efficiency is now set at 25.2 % [4]. Current research is focused on the improvement of cell stability and upscaling of the fabrication processes [6–8]. In addition, fundamental issues are elucidated and general strategies for high efficiency devices are being developed.

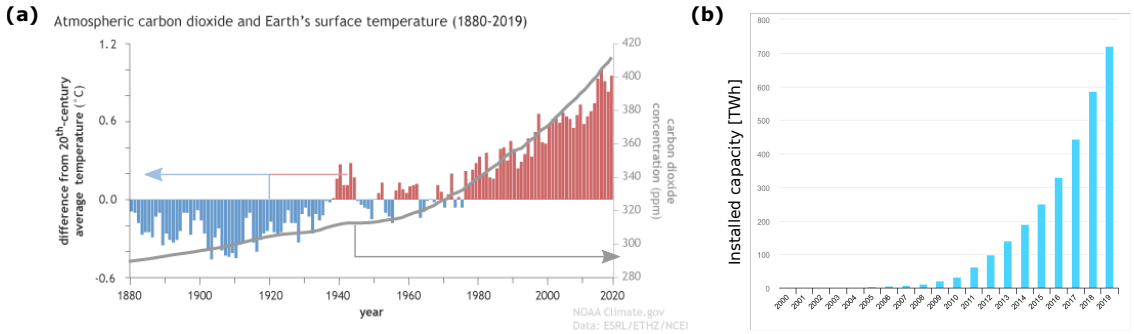

Figure 1.1: (a) Deviation of average global temperature from the 20th century average (bars, left axis) and concentration of carbon dioxide in the atmosphere (line, right axis). Reproduced from [2]. (b) Total global installed capacity of solar PV technology over the years. Reproduced from [3].

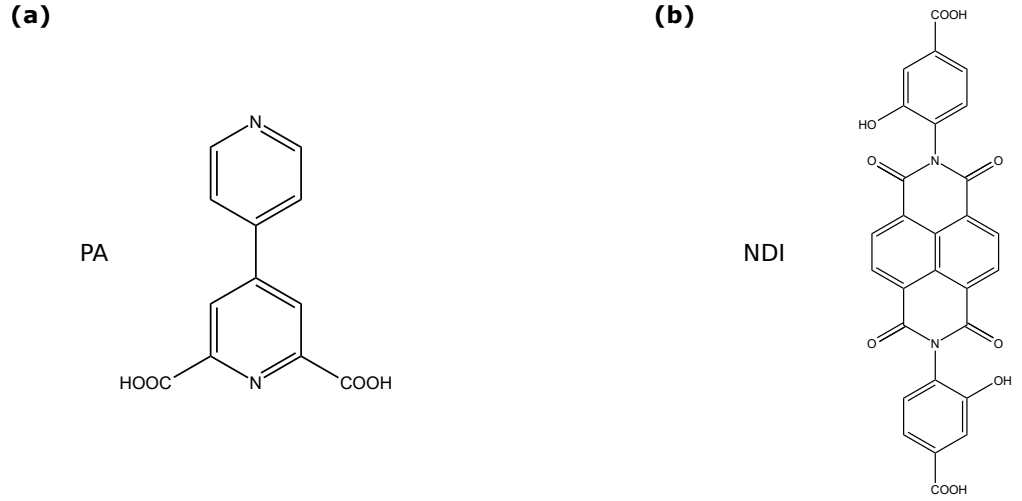

Figure 1.2: Molecular structures of the materials used in this research: (a) PA. (b) NDI.

Recently, it was shown that the presence of a molecular monolayer in between two other layers inside a perovskite solar cell can increase both the stability and efficiency of these cells [9–14]. Additionally, the use of organic molecules as interlayers allow for systematic variation of the electronic properties of the solar cells, exploiting the freedom of molecular design. In the research reported here, two different materials are tested for application in perovskite solar cells. The chemical structure of the two molecules can be found in Fig. 1.2.

In the next chapter, the working principles of a solar cell will be outlined, followed by a concise summary of the field of perovskite solar cells in Chapter 3. Then, the details of the experiments will be covered in Chapter 4, followed by a presentation and discussion of the outcome of the experiments in Chapter 5. Finally, our conclusions will be presented in Chapter 6, followed by ideas and challenges for future research in Chapter 7.

2 Theory: Working Principle of Solar Cells

2.1 Semiconductors Basics

Solar cells are able to convert the energy of sunlight into electrical energy via the photovoltaic effect, which is why they are also known as photovoltaic cells. In the photovoltaic effect, a photon is absorbed, whereby its energy is used to excite an electron to a higher energetic state.

To understand this absorption process, we need to consider the electronic properties of solids. Roughly speaking, solids can be divided into three types, based on their ability to conduct electricity: metals, semiconductors and insulators. The differences between these three can be understood via their band diagrams, as shown in Fig. 2.1. In its simplest form, a band diagram of a certain material describes the energy levels available to the electrons in that material.

Electrons will try to lower their energy as much as possible and will therefore fill up the bands in the band diagram from the bottom to the top. At absolute zero, T = 0 K, this means that N electrons will occupy the N lowest energy levels available. This situation is shown in Fig. 2.1a. When T > 0 K, thermal energy becomes available through which electrons are excited to levels with slightly higher energy. The occupation factor of a certain energy level depends exponentially on its energy and the temperature. A special energy level is the Fermi level, which is defined as the energy level with a 50 % probability of being occupied by an electron. The Fermi level is independent of temperature and for (intrinsic) semiconductors and insulators, it can be found in the middle between the valence band (VB) and conduction band (CB).

In a metal, the Fermi level is situated inside one of its energy bands, which is therefore only partially filled. In contrast, it is situated between two bands in semiconductors and insulators. In these materials, all bands below the Fermi level are completely filled, while the ones above it are empty. The first band below the Fermi level is known as the VB, whereas the first empty band is known as the CB.

From the above, the difference between a metal on one side and semiconductors and insulators on the other side is obvious. Semiconductors are distinguished from insulators based on the magnitude of the band gap (E_g): is the energetic spacing between the VB and the CB. In a semiconductor, the size of the band gap is such that at least a small fraction of the electrons in the VB can be thermally excited into the CB. An insulator however, has a band gap that is so big that no electrons from the VB can reach the CB. The distribution of electrons over the different bands in all three material types at T > 0 K, is shown in Fig. 2.1b.

To understand how the band diagram of a material affects its ability to conduct electrons, we add a positional dimension to the band diagram. This is shown in Fig. 2.2 for T > 0 K, where individual electronic states (represented by circles) are either filled (black) or empty (white). We first consider transport inside a metal. If an electron is to move, for example from site A to site B, conservation of energy requires the availability of a state with equal energy in site B. As can be seen, there are several possibilities for electron to move in this way inside the metal. Many electrons can therefore contribute to the transport of electricity and as a result, metals exhibit high conductivity.

Also in semiconductors, transport requires an empty energy level adjacent to the electron, at equal energy. For an electron in a semiconductor, to be able to move requires it to be excited from the filled VB to the empty CB. Inside the CB, there are empty levels available throughout the material,

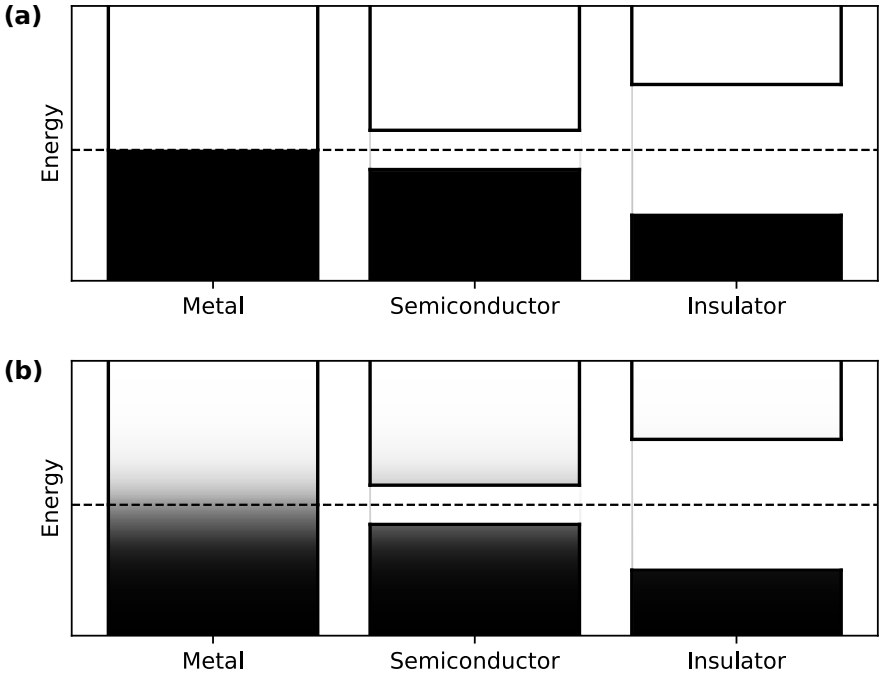

Figure 2.1: Band diagrams for a metal, a semiconductor and an insulator at absolute zero (a) and at T > 0 K. Occupation factors are visualized via a color code, where black corresponds to an occupation factor of 1 (always filled) and white corresponds to 0 (always empty). The dotted horizontal line represents the Fermi level.

allowing the electron to be transported, which can be thought of as the electron hopping from site A to B, then from B to C, and so on. The state in the VB that was previously occupied by the excited electron, is now an empty, thus allowing for electronic transport in the VB as well. In this case, electron 1 can hop from site B to A, followed by electron 2 hopping from site C to site B. This explanation of electronic transport involves the movement of multiple particles. Alternatively, charge transport in the VB can be understood using just one charge carrier, by considering the empty energy level as a particle, called a hole. The transport of the hole is depicted using the blue arrows in Fig. 2.2. The absence of an electron in this level results in a charge which is, with respect to the negatively charged background caused by the electrons, effectively positive. Missing electrons in the VB can thus be described as positively charged holes. Since both electrons and holes can be used for transport of charges, they are also known as charge carriers.

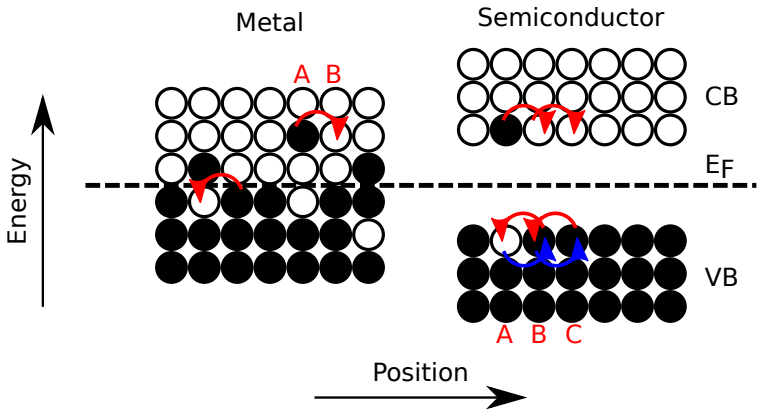

Figure 2.2: Schematic band diagram of a metal (left) and a semiconductor (right) at T > 0 K, showing how the occupation of energy levels influences the transport of charges. Empty levels are depicted as empty circles, where filled ones are filled. Red arrows correspond to moving electrons, blue ones denote the movement of holes.

Only few electrons are thermally excited in a semiconductor, resulting in only a few electrons that can be transported. Charge transport is therefore possible, but not as easy as in a metal. In an insulator, the band gap is too large for electrons to be thermally excited and therefore, conduction of electrons is not possible.

Doping

Thus far, pure semiconductors have been discussed, the properties of which are determined by the crystal structure and the distribution of atoms in that structure. These semiconductor are also known as intrinsic semiconductors. In addition, there are extrinsic semiconductors, whose properties are influenced by the presence of species that are absent in its pure form. Such species are not necessarily unwanted and are often introduced intentionally, most often with the purpose to increase the conductivity of the semiconductor material. These intentionally introduced impurities are better known as dopants.

Although generally applicable, the concept of doping will be introduced via the example of Si as the semiconductor and P atoms as the dopant (see Fig. 2.3a). When P atoms are present inside the Si structure at impurity-like concentrations, the atoms will be incorporated inside the crystal structure. However, P is a group V element and thus has one electron more than the Si atoms (group IV). Whereas four of its electrons will be involved in the bonds making up the crystal structure, the extra electron is not involved in any bonding. As a result, the energy of this electron will be different from the others and is located inside the band gap of Si, as is shown in Fig. 2.3b. In the case of P atoms inside a Si crystal, this energy level is located close to the CB minimum. Actually, it is located so close to the CB that the extra electron can be excited to the CB by thermal energy.

The thermal excitation of dopant electrons makes that the CB is more populated compared to the case of the intrinsic semiconductor. As a result, the conductivity of the material is increased significantly. Additionally, the Fermi level of the material is shifted towards the CB. Dopants that, such as P in Si, donate an electron to the CB are know as n dopants and semiconductors doped with n-dopants is a n-type semiconductor Exactly the same reasoning can be applied to dopants with one electron less than Si, so called p-type dopants. In resulting p-type semiconductors, the conductivity is increased by partial emptying of the VB and the Fermi level is shifted to to lower energy (see Fig. 2.3c).

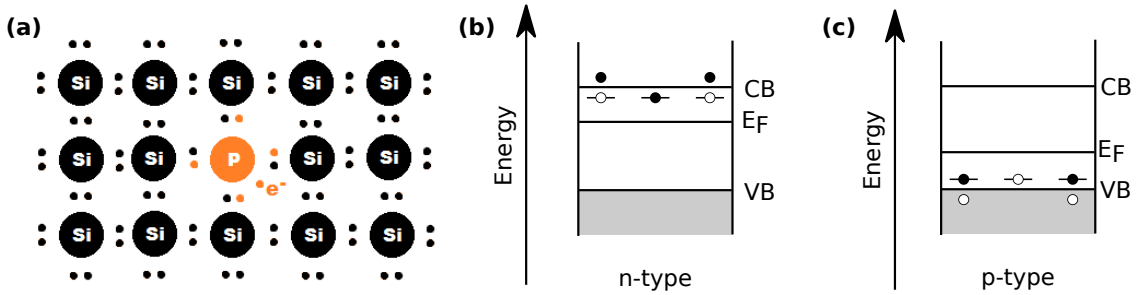

Figure 2.3: (a) Schematic picture of the crystal structure of Si, containing a P dopant atom in orange. Image reproduced from [15]. (b) and (c) show the band diagrams of n- and p-type semiconductors, including the energy levels of the dopants. Note that the Fermi level is shifted with respect to the case of an intrinsic semiconductor.

Distribution of charge carriers within a band

In most cases, when excited charge carriers are discussed, it is said that they have energies equal to their band edges. For example, electrons excited to the CB of a semiconductor are said to have an energy equal to E_c. This is however, an approximation: at finite temperatures ($T \neq 0\,K$), excited carriers have a range of energies, the exact shape of which is determined by properties of the semiconductor and Fermi-Dirac statistics. The resulting distribution of electrons is shown in Fig. 2.4 and shows that the number of electrons with a certain energy n(E) decreases exponentially with increasing energy E, according to:

$$n(E) \propto e^{-(E-E_F)/k_BT}, \tag{2.1}$$

where k_B is the Boltzmann constant and T is the temperature. The exponential decay explains why for most cases, all electrons in the CB can be said to have energy equal to band edge energy. The value of n(E) decreases so rapidly with increasing E that the energy range in which the majority of the electrons can be found, is only small in comparison to the band gap energy. From Equation (2.1), it follows that the total number of electrons with $E \geq E_i$ can be found via

$$n(E \geq E_i) = \int_{E_i}^{\infty} n(E)dE \propto e^{-(E_i-E_F)/k_BT}. \tag{2.2}$$

Additionally, for the ratio between two different energies E_A and E_B, we find

$$\frac{n(E \geq E_A)}{n(E \geq E_B)} = \frac{e^{-(E_A-E_F)/k_BT}}{e^{-(E_B-E_F)/k_BT}} = e^{(E_B-E_A)/k_BT}. \tag{2.3}$$

The last equation will prove to be useful, since it allows for calculation of n(E) at any energy level once its value on a certain energy is known.

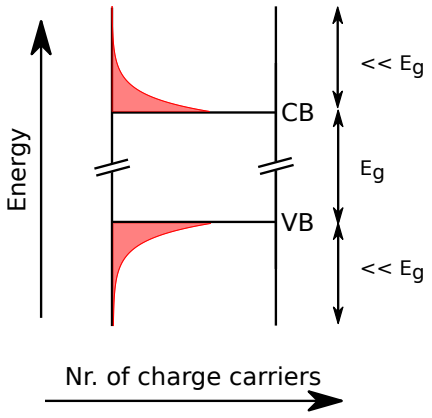

Figure 2.4: Band diagram showing the distribution of charge carriers inside their respective bands (in red). Note the interrupted vertical axis.

Light and semiconductors

Thermal excitation is not the only pathway through which electrons can be promoted from the VB to the CB. Also the energy of photon can be used to excite an electron: the fundamental reason that allows semiconductor-based solar cell devices to exist. Conservation of energy does impose a requirement on this process: the photon must provide all the energy needed to excite the electron. Upon excitation, the photon is absorbed by the material. To understand the process of

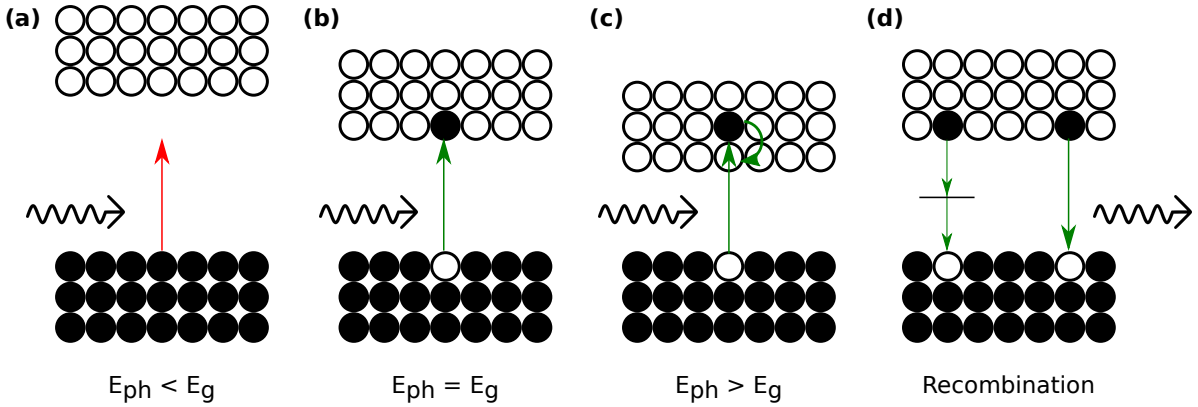

Figure 2.5: The interaction between photons and a semiconductor. Photons are represented by the wavy arrow. In (a), the band gap of the semiconductor is too large for absorption to occur. In (b) and (c), absorption is possible and different types of excitation are shown. In (c), thermalisation is also shown bent arrow). In (d), the processes of non-radiative (left) and radiative recombination (right) are schematically depicted.

light absorption, we consider the interaction of a semiconductor with a band gap E_g and a photon with different energies E_{ph} (see Fig. 2.5).

In the first case, where $E_{ph} < E_g$, no absorption occurs since the photon only has enough energy to raise the energy of the electron to a position inside the band gap, where there are no states available. Light with this energy will therefore not interact with the semiconductor and is transmitted. If $E_{ph} = E_g$, the photon has just enough energy to excite an electron from the top of the VB to the bottom of the CB. For higher photon energies, as depicted in Fig. 2.5c, different transitions can occur depending on the energy of the electron in the VB. In this case, it might be possible for the electron (or hole) to lower its energy without switching bands. The processes through which this occurs is known as thermalisation. During thermalisation, the electron (hole) lowers it energy until $E_{elec} = E_c$ ($E_{hole} = E_v$), whereby the generated energy is released as heat. Thermalisation is extremely fast and occurs on a time scale of picoseconds ($= 10^{-12}$ s) [16].

An electron promoted to the CB does not stay there forever, after some time it will return to the VB. In the end, this is were its energy is the lowest. When a electron returns to the VB, it fills up a hole which is why this is known as electron-hole recombination, or just recombination for short. This process can occur with simultaneous generation of a photon, in which case it is called radiative recombination. Radiative recombination is the reverse process of light absorption. Since radiative recombination is much slower than thermalisation, the electrons and holes involved in it have energies approximately equal to their band edges and the emitted photons have energies $E_{ph} = E_g$. Additionaly, recombination can also occur without a photon being generated. In this case, the recombination is often assisted by the presence of energy levels inside the band gap. Such levels are introduced by defects and impurities. Defect-assisted is a form of non-radiative recombination. Another example of non-radiative recombination is Auger recombination, on which more information can be found in [16]. The processes of both non-radiative and radiative recombination are shown in Fig. 2.5d.

Band gap and the solar spectrum

As explained above, the band gap of a material determines the minimum energy a photon must have to be absorbed. This has major implications for the application of semiconductors in solar cell technology. The energy of a photon is inversely related to its wavelength λ via $E_{ph} = hc/\lambda$, where h is Planck's constant and c is the speed of light. This means that photons in blue light ($\lambda \approx 470$ nm, $E_{ph} = 2.6$ eV) have more energy than their red counterparts ($\lambda \approx 700$ nm, $E_{ph} = 1.8$ eV). A semiconductor with a band gap $E_g = 1.5$ eV, will thus be able to absorb both blue and red photons,

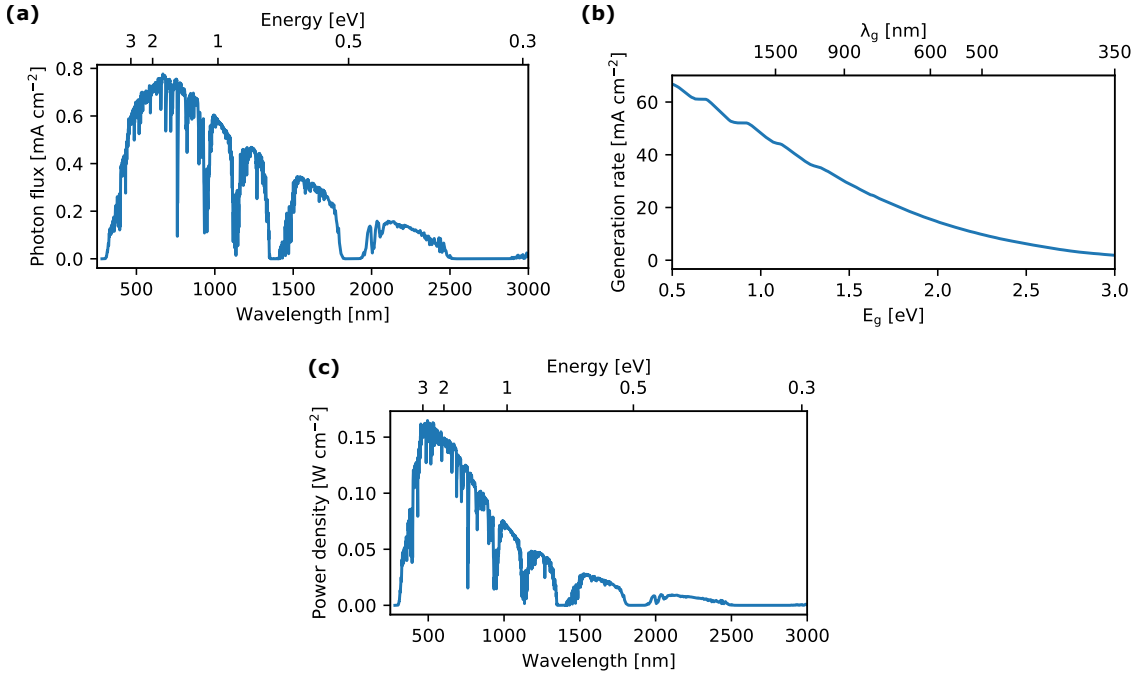

Figure 2.6: The solar spectrum in terms of the number of photons as a function of photon wavelength (a). The dependency of the generation rate on the band gap of the semiconductor (b). The solar spectrum in terms of energy as a function of photon wavelength (c). Calculations were performed using python and the moethod described by [17].

whereas a semiconductor with $E_g = 2.0\,eV$ can only absorb the blue photons.

To see how the band gap of a semiconducting material influences its ability to absorb sunlight, the solar spectrum should be considered. Sunlight contains a mixture of photons with different wavelengths, ranging from the ultraviolet (UV, $< 400\,nm$), via the visible (400-750 nm), to the infrared (IR, $> 750\,nm$). As can be seen in the solar spectrum shown in Fig. 2.6a, different photons have different abundances. The dependency of the electron-hole generation rate on the band gap, assuming total absorption of photons with energy $E_{ph} \geq E_g$, is shown in Fig. 2.6b. Obviously, a smaller band gap results in more absorbed photons and therefore a larger electron-hole generation rate.

This does, however, not mean that small band gap semiconductors are most suited for application in solar cells, since solar cells in the end, are all about energy and not about photons. It is therefore not the number of photons that is important, but how much of their energy is transformed in electrical energy. Since the process of thermalisation is extremely fast, every absorbed photon effectively creates an electron-hole pair with energy E_g. As a result, there is a trade-off between generating many, low-energy electron hole pairs (small E_g) and generating less, but higher energy electron-hole pairs (large E_g). To determine the ideal band gap for solar cell applications, we consider the power density of the solar spectrum, as shown in Fig. 2.6c. It can be seen that most energy of the sunlight's energy is carried by visible light photons, already suggesting that the ideal band gap will be close to the energy of visible light photons, rather than in the far-IR ($\lambda > 2000\,nm$) or the UV region of the spectrum ($\lambda < 400\,nm$).

Quantification of the performance of a solar cell is performed through the power conversion efficiency (PCE), also referred to simply as the efficiency. The PCE is defined as the ratio between the (maximum) power density extracted from the cell and the power density put into the device. Most typically, the integrated power density of the solar spectrum, which equals $100\,mW/cm^2$, is used for the latter [18]. In 1961, William Shockley and Hans J. Queisser were the first ones to publish on the maximum efficiencies that can be achieved for solar cells [19]. They calculated the

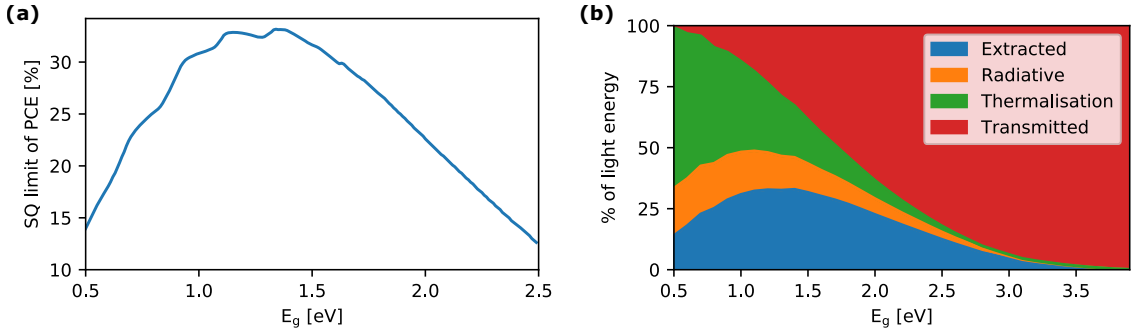

Figure 2.7: (a) The Shockley-Queisser limit for solar cell efficiencies for semiconductors with band gaps ranging from 0.5 to 2.5 eV. (b) The magnitude of different loss mechanism as a function of semiconductor band gap. For details of the calculations, see Chapter 4.

PCE achievable in ideal solar cells, commonly referred to as the SQ limit. In an ideal solar cell, the only three occurring processes are the ones introduced above: light absorption, thermalisation and radiative recombination. Since in a real solar cell, there are multiple ways for electron-hole pairs to recombine, the SQ limit present an upper limit for solar cell efficiency.

Fig. 2.7a shows how the SQ limit PCE depends on the semiconductor band gap. Efficiencies of more than 30 % can be obtained with band gap in the range of 1.0-1.6 eV and two maxima can be observed: 32.85 % at E_g = 1.15 eV and 33.16 % at E_g = 1.34 eV. In Fig. 2.7b, the influence of the different loss mechanisms on the PCE limit is shown for a range of band gap energies.

2.2 Charge Separation in Semiconductor

In the above, it was shown how the process of light absorption can be used to convert the energy of a photon into electrical energy. For this energy to be used however, the high energy electrons need to be extracted from the semiconductor, and fed into an external load that allows for a useful consumption of the electron energy. Examples of external loads include batteries, generators and light emitting diodes (LEDs).

In its most simple form, an electronic circuit is formed by connection of the semiconductor to two metals, via which it is connected to the external load. Inside the semiconductor, the excited electron travel to one of the metal contacts, called the cathode, to be extracted from the semiconductor. Via the metal, it goes to the external load, where it releases its energy, after which it is injected back into the semiconductor via the other metal contact (the anode). Alternatively, one could say that the hole leaves the semiconductor via the anode and recombines with the electron in the external load, where the energy of recombination is used to perform work. To understand the effect the metal contacts have on the transport of charge carriers inside the semiconductor, we have to compose a band diagram describing this situation.

The band diagrams of the different components, before contact, are shown in Fig. 2.8a. Compared to the band diagrams shown before, there are two additional energy levels: E_{vac} and E_{ref}. E_{vac} corresponds to the energy of an electron in vacuum, just outside the material. E_{ref} is an arbitrary but constant energy level that is allows for referencing of all other energy levels.

We now investigate what happens to the band diagram upon contacting of the three materials. A requirement for thermodynamic equilibrium is for the Fermi level E_F to be equal throughout all of the connected materials. Since in the current case, the Fermi levels of all three materials are different, charges will flow between the three parts of the system until thermal equilibrium is reached. Hence, electrons will flow from metal C to metal A until the Fermi level is constant. The band diagram describing the system in equilibrium is shown in Fig. 2.8b. It can be seen that in the semiconductor, the VB and CB have been tilted with respect to the semiconductor-only case. This tilt is induced by the internal electric field, which is turns is a result of the difference between the Fermi levels of the two metals. Quantitatively, this built-in potential V_{bi} equals $E_{F,C} - E_{F,A}$.

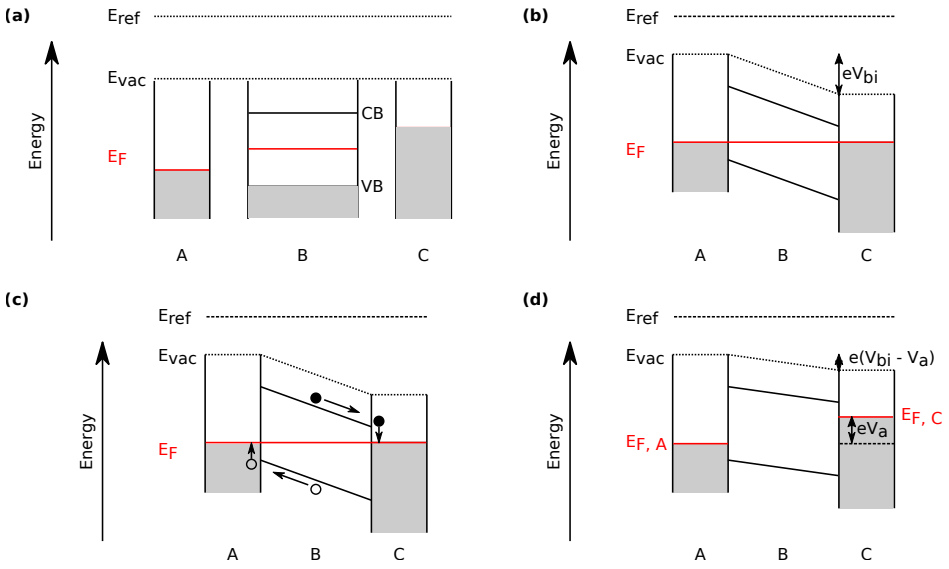

Figure 2.8: Band diagram of a semiconductor sandwiched between two different metals, in various situations. The band diagrams of the individual materials are shown in (a), the band diagram of the combined structure is shown in (b). In (c), the process fo charge extraction under short-circuit conditions is shown. The effect of an applied voltage V_a is shown in (d).

Consider now the generation of an electron-hole pair inside semiconductor B (Fig. 2.8c). Immediately after the excitation, the electron to will travel to metal A, whereas the hole will go to metal C. This type of transport, where the driving force is an electric field, is known as drift. Inside the metal, thermalisation quickly changes their energy to their initial one: that of the Fermi level. This means that all absorbed energy is already lost and no work can be performed via the recombination of the electron-hole pair. This situation is known as short-circuit and the corresponding extracted current is known as the short-circuit current J_{sc}.

One has the possibility of applying a voltage between the two metal contacts, which allows for a change in the Fermi level of one metal compared to the other. Since now there is no more equilibrium, the Fermi level does not have to be equal throughout the system. If metal A is grounded, the Fermi level of metal C can be increased by the application of an external voltage V_a, as is depicted in Fig. 2.8d. The decrease in $E_{F,C}$ results in an electric field with opposite sign to that of the built-in potential, effectively reducing the tilt of the bands in the semiconductor. Considering again the generation of an electron-hole pair in the semiconductor now leads to an energy difference $E_{F,C} - E_{F,A} = eV_a$ between the electron and the hole, once inside the metal contacts. Now, part of the photon's energy is still left and can be used to perform work. With the application of the voltage however, the driving force for the charge carriers to move to the contacts has decreased. As a result, more of the generated electron-hole pair will recombine before reaching the contacts, meaning that the number of extracted electrons is decreased with respect to the situation without an applied voltage.

In the case where the applied voltage completely cancels the built-in voltage, $V_a = V_{bi}$, the tilt of the semiconductor bands has disappeared. Because of that, there is no driving force that directs the charge carriers to their respective contacts. Now, holes are as likely as electrons to reach metal A and as a result, the net current through the system is zero. This particular case is known as open circuit and the corresponding voltage is known as the open-circuit voltage V_{oc}.

The model discussed above is known as the metal-insulator-metal model. It present a minimal but complete example of a solar cell circuit. In reality however, solar cell devices have more complicated structures for the simple reason that those allow for higher efficiencies to be achieved. In the following sections, (some of) these configurations will be introduced.

The p-n junction

The most widely applied method to separate charges in solar cells is that of the p-n junction. The p-n junction is the working mechanism on which crystalline Si solar cells are based. We first consider a p-n homojunction, which is a junction between two semiconductors of the same material, one of which is n-doped, while the other is p-doped. The case of the p-n heterojunction is similar and will be covered briefly.

The band diagrams of the two separated materials is shown in Fig. 2.9a. It can be seen that all energy levels are identical in the two cases, except for the Fermi level. Upon contacting of the two materials, there are large concentrations differences between the two semiconductors: the n-type material contains excess electrons, whereas the p-type material has a surplus of holes. This imbalance in charge carriers is expressed by the different Fermi levels. The result is the existence of diffusion currents that transport electrons from the n-type to the p-type material. Holes move in the opposite direction.

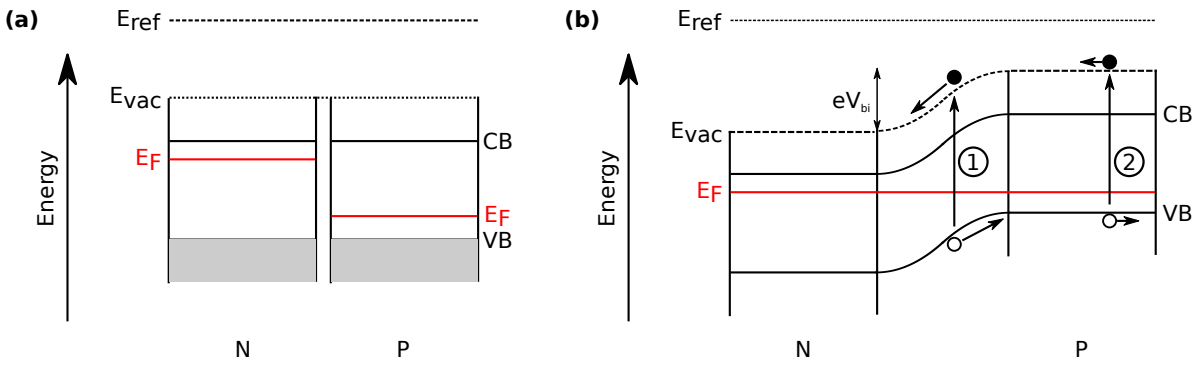

Figure 2.9: (a) Band diagrams of two pieces of a certain semiconductor material, one of which is n-type (left), the other p-doped (right). (b) Band diagram of the structure after contacting of the two materials, showing the induced bending of the bands and the resulting depletion region.

Since the charge carriers mentioned above originate from the static dopants, they result in the exposure of the ionized dopant ions. These ions change the band structure of the junction in such a way that the charge carriers are kept inside the material where they are the majority carrier (see Fig. 2.9b). The exact way the bands are bended at the junction can be determined mathematically and follows from the consideration that the ionized dopants induce an electric field across the junction. The calculation itself is not performed here, but can be found in [16]. It can be seen that generated built-in voltage drops within a small region of the p-n junction, which is known as the depletion or space-charge region. Outside of the depletion region, the concentration of majority carriers is assumed to be approximately equal to that of the isolated doped materials and these regions are therefore referred to as 'quasi-neutral'.

We can consider now two different pathways for charge carrier extraction, depending on the location of the electron-hole pair generation. First, we consider the absorption of a photon inside the depletion region (1 in Fig. 2.9b). The electrons and hole generated in this region are subjected to an electric field that causes them to separate and drift towards their contacts: the electron enters the n-type material, while the hole enters the p-type material. Since now both the hole and the electron are the majority carrier, they have a high conductivity and are expected to reach their metal contact.

Secondly, electron-hole pairs can be generated in the quasi-neutral regions (Fig. 2.9b, 2). Whether this electron-hole pair will be extracted or recombine inside the semiconductor, depends on whether the generated minority carrier reaches the junction before it recombines. For the transport towards the junction, the minority carrier has to rely on diffusion, driven by the depletion of minority carriers close to the junction. In the meantime, recombination with one of the majority carriers can lead to its annihilation.

Heterojunctions

Semiconductor junctions are not necessarily formed by two pieces of the same semiconductor material. The two sides of the junction may very well correspond to different materials, resulting in different types of junctions, depending on the band gap and doping of the two semiconductors. In the following, the band diagram of a p-n heterojunction will be tentatively introduced.

Consider a n-doped semiconductor (N) and a p-doped semiconductor (P) with band gaps and Fermi levels such that $E_{g,\,N} > E_{g,\,P}$, $E_{v,\,N} < E_{v,\,P}$ and $E_{c,\,N} < E_{c,\,P}$ (see Fig. 2.10a). Upon contacting the two materials, we can expect the following things to happen, based on the analogy with a p-n homojunction: first, majority carriers will diffuse across the junction two equalize the Fermi levels on both sides of the junction. By doing so, they leave behind unscreened, ionized dopant atoms that will result in the buildup of an electric field opposing the diffusion of the majority carriers. So far,

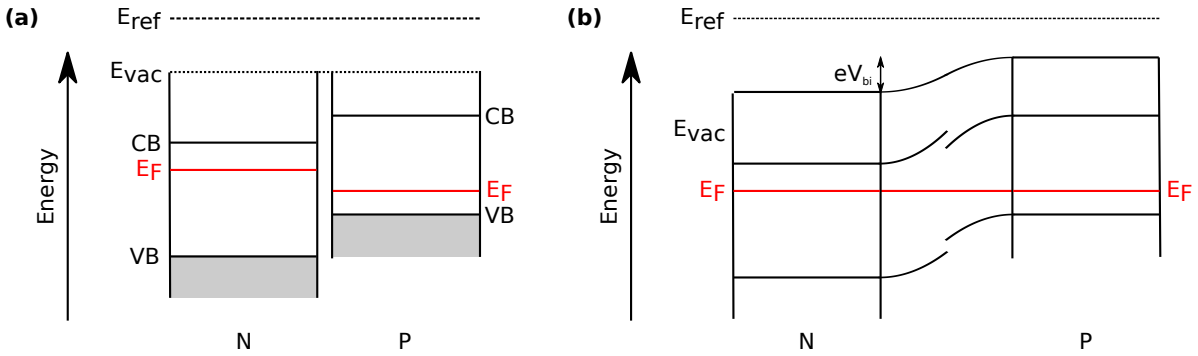

Figure 2.10: (a) Band diagrams of two semiconductor materials with opposite doping types. (b) Band diagram of the structure after contacting of the two materials, showing the induced bending of the bands and the discontinuity of the bands at the junction.

the analogy of with the p-n junction holds perfectly, since the only requirements for the described process of band bending are inequality of the Fermi levels (1) and for the semiconductors to be doped (2). As a result of the electric field that is induced by the unscreened dopants, the bands of the semiconductors will bend.

The band diagram of the p-n heterojunction discussed here, is shown in Fig. 2.10b. One can see that the bands bend in a similar manner to the case of the p-n homojunction, except for the presence of discontinuities in the VB and CB, exactly at the junction. These discontinuities are a consequence of the fact that the bending of the VB and CB in a certain material is identical: if the energy of the VB increases by ΔE inside the depletion region, the energy of the CB must change by the same ΔE. For the bands to be continuous, the band bending of the CB due the presence of the built-in field, should be more severe than the bending of the VB in the presence of the same field, which is not possible. The discontinuities can be quantified and are equal in magnitude to the differences between the band levels of the individual semiconductor materials (see also Fig. 2.10b). This also shows that for vanishing energy differences, we return to the case of the p-n homojunction.

p-i-n junction

As was discussed during the introduction of the p-n junction, the most optimal position for an electron-hole pair to be generated, is inside the depletion region. Excitation in this region is immediately followed by drift of the two charge carriers away from each other, because of the built-in electric field. In contrast, extraction of photogenerated charge carriers inside the quasi-neutral regions is less probable. A more effective situation would be one in which the same amount of photons would be absorbed, but then exclusively inside the space-charge region. This requires an increased size of the space-charge region (1) and minimized absorption in the quasi-neutral regions (2). A p-i-n junction does exactly that: the use of an intrinsic semiconductor (the 'i' in p-i-n), in which there are no dopants that shield the built-in potential, result in an extended depletion region. The second requirement is met by the use of doped insulator materials, which absorb only few photons because of their large band gap.

The band diagram describing such a junction in thermal equilibrium is shown in Fig. 2.11a, together with the pathway of electron-hole pair generation and separation. The absence of dopant in the intrinsic semiconductor make that no band bending occurs inside this material. The bands of connected insulator materials will bend, but this is omitted for clarity. A major loss mechanism in p-n junction solar cells is the recombination of minority charge carriers that do not reach the junction. In p-i-n junction cells, photogenerated charge carriers never are minority carriers: they are generated inside the intrinsic semiconductor, in which the concept of minority and majority carriers does not apply. From there, they are transported to the doped insulators, where they

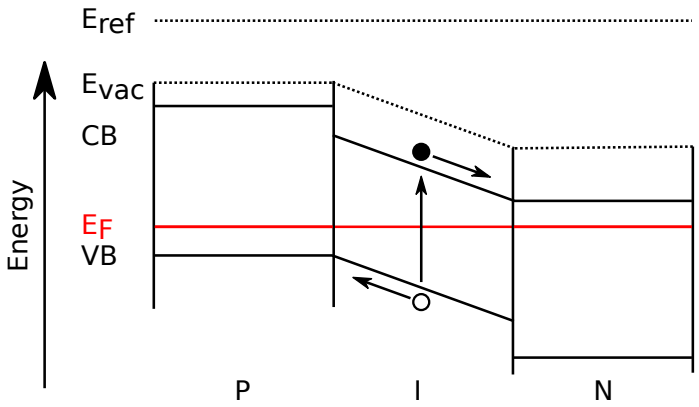

Figure 2.11: Band diagram of a p-i-n junction, showing the extended width of the depletion zone.

become the majority carriers. Additionally, the presence of the built-in voltage over the complete range where photons are absorbed allows for quick separation of electrons and holes.

Metal-semiconductor junction

Metals are well known for their superior conductivity. It is therefore, that almost every electric circuit is made out of electrical components connected via metals. This is not different with solar cells and transfer of electrons or holes from a semiconductor or insulator is the last step in the process of charge extraction from the solar cell. It is therefore that the concept of metal-semiconductor junctions is introduced here.

We consider a metal that is to be contacted with a n-type semiconductor to explain, in general, the characteristics of a metal-semiconductor junction. Junctions between a metal and a p-type semiconductor or insulators can be described in analogy. In Fig. 2.12a, the band diagrams of the individual components are shown. When the two materials are contacted, electrons will flow from the the n-type semiconductor to the metal, in order to equilibrate the Fermi level throughout the junction. As was the case during the formation of the p-n junction, the transfer of electrons to the metal results in the presence of unshielded, ionized dopants. These dopants introduce an internal electric field that will bend the VB and CB of the semiconductor, resulting in a band diagram such as shown in Fig. 2.12b. Therefore, in the resulting band diagram, there is a barrier that opposes any charge flow between the semiconductor into the metal. What the height of this barrier is, depends on the direction in which an electron is to cross the junction. Going from the metal to the semiconductor, its height $\Phi_B = E_{F,\,M} - E_{C,\,S}$. The other way around, its height is equal to the built-in potential: $V_{bi} = E_{F,\,N} - E_{F,\,M}$. The parameter Φ_B is commonly referred to as the Schottky barrier height.

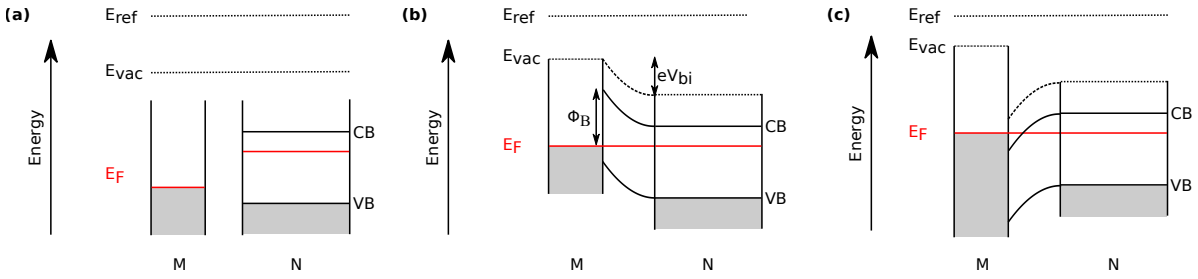

Figure 2.12: (a) Band diagrams of a metal and a n-type semiconductor. (b) Band diagram of the metal-semiconductor junction formed by contacting of the two materials shown in (a). (c) Band diagram of a metal-semiconductor junction where an ohmic contact is formed.

Upon application of an external bias V_a, the band diagram changes and the potential experienced by electrons going from the semiconductor to the metal changes to $(V_{bi} - V_a)$. In contrast, the height of the Schottky barrier is not affected by the applied potential.

In the extrinsic semiconductors and insulators used in solar cells, the dopant concentrations can be very high. Since the width of the depletion region decreases with increasing doping levels, this can result in a depletion region that is thin enough to allow for quantum mechanical tunneling of the electrons. One could say that the barrier is so thin, that is has become leaky. In that case, electron transfer between the semiconductor and the metal can be very easy and the contact is said to be ohmic.

Another way in which an ohmic contact can be formed, is by the combination of a metal and a semiconductor for which $E_{F,\,M} > E_{C,\,N}$ holds. As can be seen from the band diagram shown in Fig. 2.12c, this results in a configuration in which electron transfer from the semiconductor to the metal is energetically downhill. A consequence of the contact being ohmic is that the Fermi level of the metal and the semiconductor will be equal, even upon application of an external bias.

Diode equation

Most of the junctions introduced above, have rectifying properties, meaning that for at least one of the charge carriers, the conductivity throughout the junction is dependent on the direction of transport. The rectifying properties of these junctions result in asymmetric current-voltage behaviour: $J(V_a) \neq -J(-V_a)$. This is in contrast to the current-voltage behaviour of an ohmic junction (see Fig. 2.13a). To understand the shape of the $J - V$ curve, we need to investigate the charge carrier transport at the junction.

Consider the partial band diagram of a general junction at equilibrium ($V_a = 0$), as shown in Fig. 2.13b. In the CB, the distribution of the electrons is explicitly drawn on both side of the junction. In the n-type material on the left, the majority carriers (electrons) are driven towards the junction by the difference in concentration between both sides of the junction. However, conservation of energy dictates that only those electrons for which $E \geq E_{C,\,P}$, are able to reach the other side of the junction (1). The others cannot cross the barrier and remain in the n-type material (2). As a result,

$$J_{diff}(V_a = 0) = J^0_{diff} \propto n(E \geq E_C + V_{bi}). \tag{2.4}$$

On the right side of Fig. 2.13b, the flow of electrons carrying the drift current is shown, including their energy. Transport in this direction does not require the electrons to overcome an energetic barrier and it is therefore that all electrons are able to enter the n-type material (3).

In equilibrium, the net current is zero, since the drift current cancels out the diffusion current:

$$J^0_{tot} = J^0_{drift} + J^0_{diff} = 0. \tag{2.5}$$

Next, we consider the same junction, but now in the presence of an external bias, as shown in Fig. 2.13c. The applied potential decreases the barrier by V_a, resulting in a total barrier $V_{tot} = V_{bi} - V_a$. Considering again the electrons that attempt to diffuse into the p-type region, now results in more electrons being able to travel across the junction, because of the decreased barrier height. In this case,

$$J_{diff}(V_a) \propto n(E \geq E_C + V_{tot}) = n(E \geq E_C + (V_{bi} - V_a)). \tag{2.6}$$

Making use of the ratio formula in Boltzmann statistics (Equation (2.3)), we find

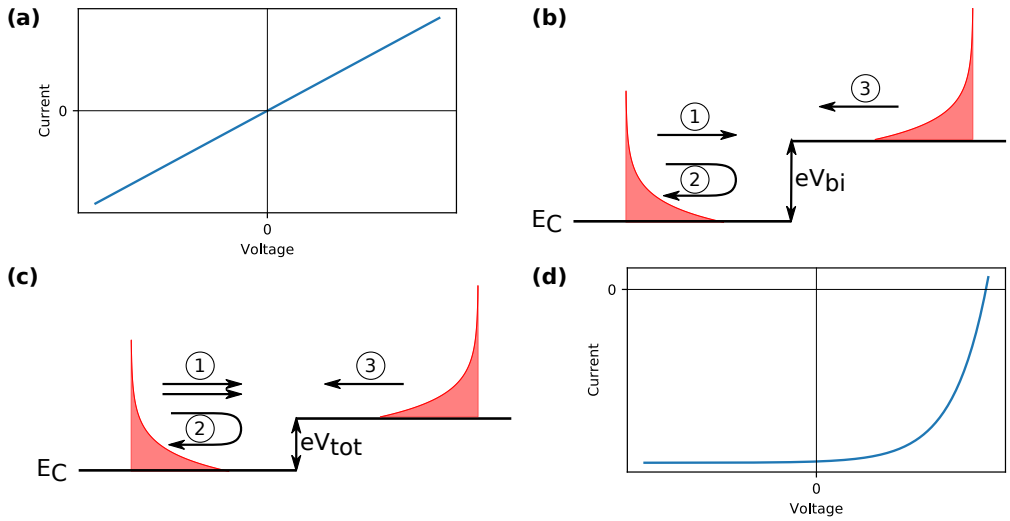

Figure 2.13: (a) J – V curve of an ohmic junction. (b) Partial band diagram showing a conduction band close to a junction, where the exact shape of the junction is not defined. Distribution of charge carriers within this band is shown in red. (c) The diagram of (b) but now with the application of an external bias which lowers the height of the junction. (d) J – V curve of an illuminated diode.

$$\frac{J_{diff}(V_a)}{J^0_{diff}} = \frac{n(E \geq E_C + (V_{bi} - V_a))}{n(E \geq E_C + V_{bi})} = e^{(V_{bi} - V_a - V_{bi})/k_B T} = e^{V_a/k_B T} \tag{2.7}$$

For the drift current on the other hand, all electrons are still able to traverse the space-charge region and reach the n-type material:

$$J_{drift}(V_a) = J_{drift}(V_a = 0) = J^0_{drift}. \tag{2.8}$$

By combining Equation (2.7) and Equation (2.8), the total current becomes:

$$J_{tot} = J_{diff} + J_{drift} = J^0_{diff} e^{V_a/k_B T} + J^0_{drift}. \tag{2.9}$$

Using the fact that the drift and diffusion current in the absence of a voltage are equal but of opposite sign (Equation (2.5)) and rearrangement of terms yields:

$$J_{tot} = J_{diff} + J_{drift} = J^0_{diff} e^{V_a/k_B T} - J^0_{diff} = J^0_{diff}(e^{V_a/k_B T} - 1). \tag{2.10}$$

Equation (2.10) is known as Shockley diode equation and describes the current-voltage characteristics of idealized diodes.

In the presence of light, the generation of electron-hole pair will influence the shape of the J – V curve with respect to the dark situation. We have seen already before, that without the application of an external bias ($V_a = 0$), a current J_{sc} flows through the junction that consist of light generated charge carriers influence by the internal electric field. This current can be added to the derived expression for diode in the dark (Equation (2.10)) to yield an expression for the J – V behaviour of illuminated diodes:

$$J_{tot} = -J_{sc} + J^0_{diff}(e^{V_a/k_B T} - 1). \tag{2.11}$$

3 Background: Perovskite Solar Cells

The research field of perovskite solar cells has its roots in te field of dye-sensitized solar cells (DSSCs). The first report on the use of perovskites in a solar cells was in the configuration of a DSSC: nanoparticles of lead halide perovskite were used as sensitizers [5]. Later on, solid-state versions of these perovksite DSSCs, where the liquid HTM was replaced by a solid molecular material (Spiro-OMeTAD), were shown to be superior in terms of efficiency [20, 21]. Also, the need for a mesoporous electron transport material was found to be unnecessary [21]. Therefore, the structure of a perovskite solar cell is build up from the following layers, starting from the side exposed to incident light: transparent conductive oxide, selective transport layer, perovskite, oppositely selective transport layer, metal electrode. As already suggested by the word layer, the different components of the cell can be thought of as planar layers, see also Fig. 3.1. In terms of working mechanism, perovskite solar cells are best described by the p-i-n junction [7]. In what follows, the different components of perovskite solar cells will be introduced, together with some properties of these cells.

3.1 Lead halide perovskites

In the context of solar cells, the name perovskite refers to the perovskite crystal structure of the used semiconductor material. Although the original perovskite mineral is $CaTiO_3$, the perovskite materials used for solar cell applications are made out of completely different elements: lead and halides. The most typical example of a lead halide perovskite material is methylammonium lead iodide ($CH_3NH_3PbI_3$, $MAPbI_3$). This material was used in the pioneering works of the field and still serves as a model compound. The crystal structure of $MAPbI_3$ consists of alternating $[PbI_6]$ octahedra and MA^+ ions resulting in a nearly cubical structure (see Fig. 3.1). This material is characterised by a high absorption coefficient ($> 10 \times 10^5\,cm^{-1}$) [22] and a bang gap of 1.55-1.60 eV [7]. Consequently, the SQ limit for the PCE is 30.1 % [17]. There is however, a certain degree of freedom concerning the band gap. The band gap of perovskite materials is dependent on its composition, the band gap of $MAPbBr_3$ for example, is 2.3 eV [23]. Via the concept of solid solutions, the band gap of $MAPbI_xBr_{1-x}$ can be continuously varied from 1.6 eV to 2.3 eV, depending on the value of x. A similar thing can be achieved by (partial) substitution of the MA cation, although the effects of this are less severe.

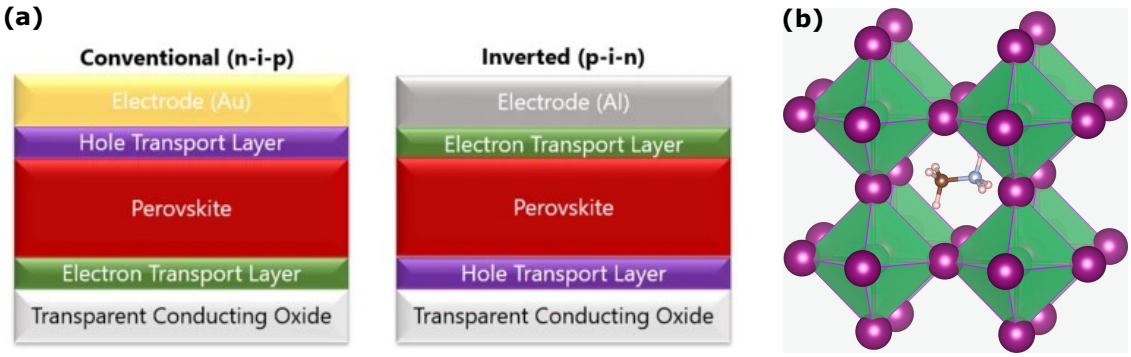

Figure 3.1: (a) Configuration of perovskite solar cells, which differ in the position of the selective layers. Reproduced from [24]. (b) Unit cell of $MAPbI_3$. Reproduced from [25].

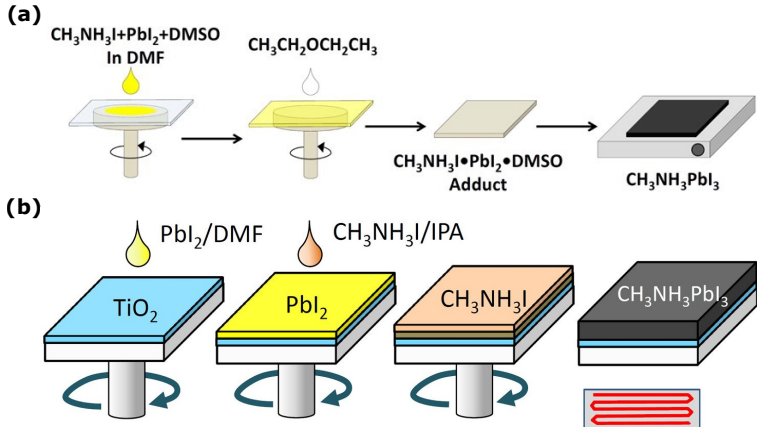

Figure 3.2: Drawings showing the different steps of the one-step (a) and two-step (b) preparation method for perovskites. Adapted from [27] and [29], respectively.

Typically, semiconductor materials in solar cell applications require high purity and excellent crystallinity, since the presence of any imperfection in its structure affects its performance detrimentally. This is because any defects will lead to the introduction of energy levels inside the band gap, which will act as non-radiative recombination sites. However, perovskites layers with relatively small grain sizes can still exhibit high PCE values. The reason for this defect tolerance lies within its electronic structure. Imperfections, such as a missing I^- ion, result in the appearance of energy states inside the VB and/or CB [26]. Non-radiative recombination from such states will then be largely suppressed, allowing for well performing solar cells in the presence of defects.

For the preparation of the perovskite layer, roughly two methods can be distinguished. Both of them employ spin coating to create the layers, but differ in the amount of spin coating steps. The two methods are conveniently referred to as the one-step and the two-step method. In the one-step method, equal molar amounts of PbI_2, MAI and DMSO are mixed in a DMF solution. This solution is then spincoated on the substrate. During the spin coating process, antisolvent (typically diethyl ether) is dripped on the substrate to induce crystallisation of the material. After spin coating, a transparent film is obtained that corresponds to a $MAI \cdot PbI_2 \cdot DMSO$ adduct [27]. During the subsequent annealing process, this phase is transformed into the perovskite structure by evaporation and a black film is obtained. Alternatively, in the two-step method, a layer of PbI_2 is first coated onto the substrate, after which it is converted into $MAPbI_3$ by a second coating step using a MAI solution [28].

In Chapter 2, we have seen how ionized species can influence the band diagram of materials and junctions. The ions in that case, we dopants that were incorporated into the lattice and said to be static. In perovskites, things are slightly different. By means of DFT simulations, it was calculated that iodine ions have only a small energetic barrier of 0.58 eV for hopping into an available site (a vacancy) [30]. This allows these vacancies to move at ambient temperatures, but only slowly. In the presence of an electric field, such as that generated by a built-in potential or one externally applied, these vacancies will be transported in one particular direction [31]. Being ions, they affect the shape of the band diagram and as a result, the band diagram of perovskite layers is dependent on the ion vacancy distribution. A detailed discussion on this can be found in [32]. Here, we will directly jump to the consequences: equilibration of perovskite solar cells at applied voltages V_a higher than the builtin voltage V_{bi} leads to improved performance compared to devices equilibrated at $V_a < V_{bi}$. Since the movement of ions is rather slow, $J - V$ curves show different behaviour depending on the history of the device. As can be seen in Fig. 3.3, this leads to a hysteresis between two scans obtained after each other.

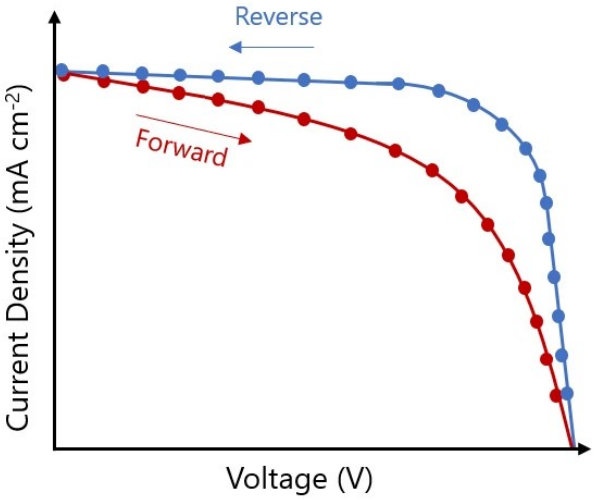

Figure 3.3: J – V curve showing the different behaviour depending on the scan direction. Reproduced from [24].

3.2 Selective transport layers

In perovskite solar cells, the absorber is sandwiched by two layers that are selective for one specific charge carrier. These layers are also known as the electron and hole transport materials (ETM and HTM). Depending on the orientation of the p-i-n junction with respect to the contacts, the final configuration is said to be of the pin or nip type. Herein, nip corresponds to transparent conductive oxide / ETM / perovskite / HTM / metal contact. For the pin configuration, the ETM and HTM are interchanged. In the research performed, only the nip configuration was used and the materials used in it will therefore be introduced.

In the nip configuration, light will have to pass through the ETM before it reaches the absorber layer. It is therefore that the ETM material is chosen to have a large band gap. The most popular choices for ETMs have been metal oxides, especially TiO_2, SnO_2 and ZnO. Although the use of titania as the ETM is established, a result from the DSSC research field, its requires very high temperatures during its fabrication process (> 400 °C). It is therefore that other metal oxides have gained more attention.

ETM layers of SnO_2 can be grown using a low processing temperature of 150 °C [33]. The resulting layer, with a thickness of about 25 nm, also showed reduced hysteresis with respect to cells using TiO_2 as the ETM. For SnO_2 ETMS, it has been suggested that the energy alignment with the perovskite layer is better than that of TiO_2 (see Fig. 3.4a) [34].

For the HTM material in nip configurations, also some different materials have been employed. The one which results in the highest efficiencies however, is a molecular material known as Spiro-OMeTAD [7]. The structure of Spiro-OMeTAD is shown in Fig. 3.4b. The conductivity of pristine Spiro-OMeTAD is however only low and therefore, it is usually doped with Li-TFSI and optionally other materials. Although the conductivity is greatly improved in this way, the stability of the layer is negatively affected. As a result, the development of other HTMs for use in perovskite solar cells is an active field of research [35, 36].

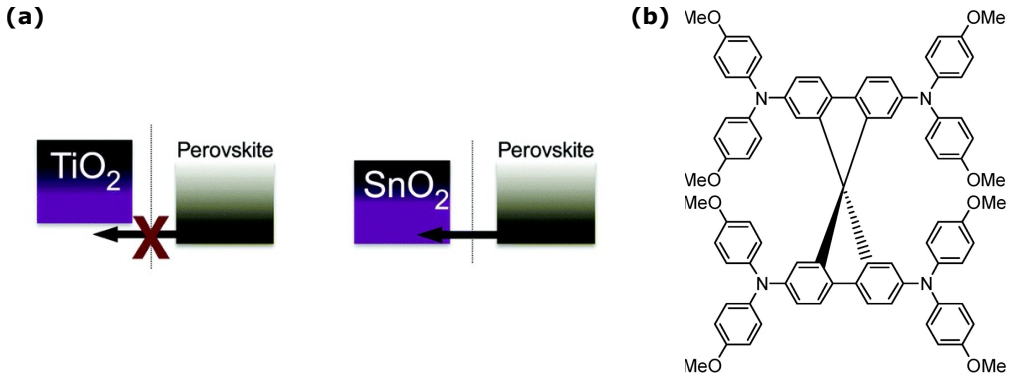

Figure 3.4: (a) Partial band diagram showing the improved band alignment for SnO_2 as the ETM. Adapted from [34]. (b) Molecular structure of Spiro-OMeTAD.

3.3 Interface modification

In perovskite solar cells, interfaces are of huge importance. First of all, the energetic structure of the interfaces can heavily influence the band diagram of a junction. As was shown, many of the transport properties are determined by the electronic properties of the junction. Secondly, interfaces are known to be an area with high recombination rates. Atoms at surfaces and interfaces are often found in decreased coordination numbers, leading to the presence of recombination sites. The third way in which interfaces influence the solar cells has to do with the fabrication process. Since one layer is deposited after the other, the last layer can influence the growth process of the next layer, for example via its wettability. It is therefore that interface modifications are attraction interest from within the research field.

An example of such an interface modification is the functionalization of the ETM surface with fullerene derivatives [11, 37]. The hydrophobic fullerene-like molecules decrease the wettability of the surface, which is believed to beneficial for the crystallisation of the perovskite layer. In another example, the interface of the ZnO ETM was modified using molecules with a large dipole moment [12]. Via their dipole moment, the molecules able to improve the band alignment between perovskite and ZnO and in that way, charge extraction was improved.

In other works, the surface of the transparent conductive oxide was modified with the goal of replacing the selective layer [13, 14]. As a result, selective layers were created that consisted of a single monolayer of molecules. By changing its structure, the energetics of the molecules can be systematically varied and the band alignment can be optimized.

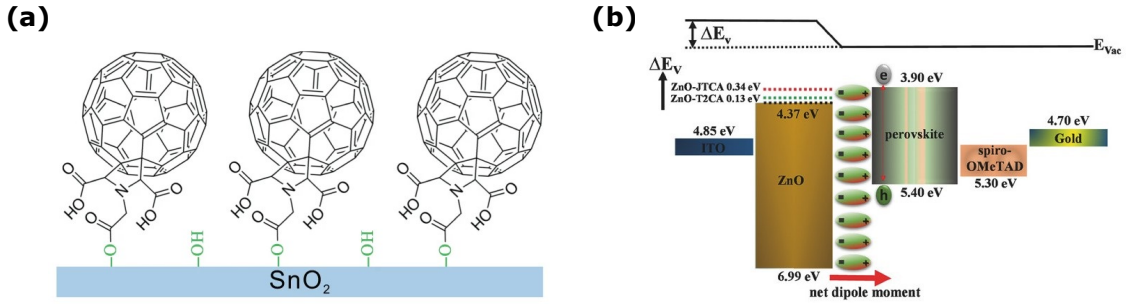

Figure 3.5: (a) Schematic showing the modification of the SnO_2 surface with fullerene derivatives. Adapted from [11]. (b) Band diagram showing how the interface modification lead to improved band alignment. Adapted from [12].

4 Methods

4.1 Materials

- 2-Methoxyethanol (2-MeO-EtOH, anhydrous, 99.8 %), Sigma-Aldrich.
- [4,4'-bipyridine]-2,6-dicarboxylic acid (PA, DN-S10), Dyenamo.
- 4-*tert*-Butylpyridine (TBP, 98 %), Sigma-Aldrich.
- Acetone (EMPLURA®, ≥ 99.0 %), Sigma-Aldrich.
- Acetonitrile (ACN, anhydrous, 99.8 %), Sigma-Aldrich.
- Chlorobenzene (CB, Extra Dry, AcroSeal™, 99.8 %), Acros Organics.
- Deionized water (DI-H_2O, ACS), Alfa Aesar.
- Diethyl ether (Et_2O, anhydrous, ≥ 99.7 %), Sigma-Aldrich.
- Dimethyl sulfoxide (DMSO, Extra Dry, AcroSeal™, 99.7 %), Acros Organics.
- Ethanol (EtOH, AnalaR NORMAPUR® ACS, Ph. Eur. Reag., ≥ 99.8 %), VWR International.
- Fluorine-doped tin oxide coated glass (FTO glass, NSG TEC™15, sheet resistance 15 Ω/sq), Pilkington.
- FK 209 Co(III) TFSI salt (DN-P04), Dyenamo.
- Hydrochloric acid (HCl, ACS reagent, 37 wt%), Sigma-Aldrich.
- Lithium bis(trifluoromethane)sulfonimidate (LiTFSI, trace metals basis, 99.95 %), Sigma-Aldrich.
- Methanol (MeOH, CHROMASOLV®, for HPLC, ≥ 99.9 %), Sigma-Aldrich.
- Methylammonium Iodide (MAI, ≥ 99 %), GreatCellSolar.
- *N, N*-Dimethylformamide (DMF, anhydrous, 99.8 %), Sigma-Aldrich. Used for perovskite precursor solutions only.
- *N, N*-Dimethylformamide (DMF, AnalaR NORMAPUR® ACS, Ph. Eur. Reag., ≥ 99.8 %), VWR International.
- PbI_2 (trace metals basis, 99.99 %), TCI Europe.
- RBS™50 concentrate, Sigma-Aldrich.
- Spiro-OMeTAD (2,2',7,7'-Tettrakis[N,N-di(4-methoxyphenyl)amino]-9,9'spirobifluorene, sublimed grade, 99.8 %), Borun New Material Technology.
- Tetrabutylammonium hexafluorophosphate (NBu_4PF_6, for electrochemical analysis, 98.0 %), Sigma-Aldrich.
- Tin(IV) oxide (SnO_2, colloidal dispersion, 15 wt% in H_2O), Alfa Aesar.
- Zinc dust (< 10 μm, ≥ 98.0 %), Sigma-Aldrich.

The NDI molecule was synthesized by colleagues from a related research group, according to an experimental method reported in ref. [38]. In the following section, several spin coating steps and UV/O_3 treatments will be mentioned. These were performed using a WS-650-23 Spin Coater (Laurell) and an E511 UV Ozone Cleaner (Ossila), respectively.

4.2 Cell fabrication

FTO glass cutting and etching

Using a glass cutting wheel and a glass cutting surface covered with millimeter paper, big FTO glass plates (30 cm x 30 cm) were patterned into rectangles with dimensions 1.4 cm x 2.4 cm, corresponding to the final device size. With special glass cutting pliers, the glass plate was broken such that a rectangular set of four by two devices was obtained (9.8 cm x 2.8 cm, seeFig. 4.1b). Using regular scotch tape, these rectangles were covered such that everything but a rectangle of 9.8 cm x 6 mm, centred at the long axis, was covered. Next, the uncovered area was covered with Zn powder, followed by a few mL of 2 M HCl (aq). After 10 min, the suspension on the FTO glass was diluted using H_2O, before being washed with H_2O and removal of the scotch tape.

Now, the FTO glasses were cleaned by sonication in a 1/90 (v/v) RBS 50/H_2O solution. After 30 min of sonication, the glass was removed from the solution, rinsed with H_2O and dried using a pressurized air flow. The above was then repeated using acetone (30 min), ethanol (30 min) and H_2O (10 min).

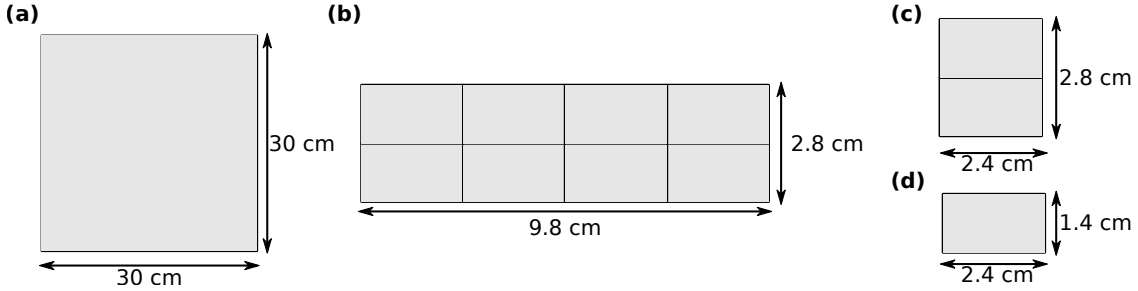

Figure 4.1: Dimensions of FTO glass plates during different stages of the fabrication process.

SnO_2 layer deposition

To prepare the substrates for the deposition of the SnO_2 layer, the outermost 3 mm of their long edges was covered with kapton tape. Using the glass cutting pliers, the glass plates were then broken into 2.4 cm x 2.8 cm rectangles, corresponding to two devices connected by their long edge (see Fig. 4.1c). Just before deposition of the SnO_2 layer, the substrates were subjected to 30 min of UV/O_3 treatment, after which the kapton tape was removed.

A SnO_2 precursor solution (~ 3 wt%) was prepared using a commercial SnO_2 colloidal solution (15 wt%), which was diluted (1:4 v/v) using DI water that pressed through a 0.45 μm filter (VRW International). Directly after the dilution step, the solution was sonicated for less than 5 min, after which is was to shake until usage. The SnO_2 precursor solution was prepared 1 h before usage, at earliest.

Deposition of the SnO_2 layer as done via a static spin coating procedure, using 300 μL of precursor solution, 3000 rpm as the rotation speed, 3000 rpm/s acceleration and a total spinning time of31 s. Directly after, the substrate was transferred to a hotplate, which was set to 150 °C. 30 min after transferring the last sample to the hotplate, the heating element was turned off. The samples were removed from the hotplate ca. 20 min after turning off the hot plate. Upon removal, the temperature

of the substrates, was 60-70 °C as determined by the temperature of the hotplate. Until further use, the cells were kept in the dark, inside a N_2 atmosphere.

NDI & PA surface modification

For the modification of all combinations of surface and surfactant, a bath deposition procedure was applied. For deposition of NDI, a 1 mM solution of NDI in DMF was used. Because of the limited amount of NDI, this solution was used for multiple depositions. It is expected the concentration does not change between deposition rounds, because only a monolayer is expected to be used. The PA solution used for the bath deposition procedures was a 0.1 mM PA solution in MeOH. At higher concentrations, PA was found not to dissolve completely.

Preparation of the substrate for the bath deposition is identical to the preparation procedure for the SnO_2 deposition, except for the removal of the kapton tape: during the bath deposition, the kapton tape was left on the cells to prevent the molecules to protect part of the substrate surface from the solution. After the UV/O_3treatment, the substrates were immersed in the molecular solutions, where they were left overnight. The next morning, they were taken out of the solution, rinsed and dried by an airflow. Also the kapton tape was removed. For PA treatment, the rinsing solvent was EtOH, whereas DMF was used for the NDI molecule.

Perovskite layer deposition

Preparation of the $MAPbI_3$ precursor solution was done in an Ar-filled glovebox. Typically, 1014 mg PbI_2 (2.2 mmol) and 318 mg MAI 2.0 mmol were added into a vial, after which 1.1 mL DMF and 0.15 mL DMSO (~ 2 mmol) were added. The vial was then taken out of the glovebox and wrapped with parafilm. To ensure complete dissolution of all components, the vial was shortly mixed using a vortex mixer and left in a shaker for at least 2 h. The perovskite solution was always prepared and used on the same day. The final PbI_2 concentration of the solution, based on the DMF volume, was calculated to be 2 M and the PbI_2 : MAI : DMSO ratio was 1.1 : 1.0 : 1.

Deposition of the perovskite layer was done using a static spin coating method, performed inside a N_2-filled glovebox. Prior to the deposition, the FTO and DFTO/SnO_2 substrates underwent 25 min of UV/O_3treatment, before being transferred into the glovebox. The spin coating was then performed using 60 μL of the precursor solution, which was spread to cover the substrate surface before coating, which was done using a rotation speed of 4000 rpm, an acceleration of 4000 rpm/s and a total spinning time of 21 s. With 13 s of spinning time left, 0.3 mL of Et_2O antisolvent was dripped onto the substrate. After spinning, the substrate was immediately transferred to a hotplate set at 100 °C, inside the glovebox, where it was left for an annealing time of 10 min.

Spiro-OMeTAD layer deposition

Doped Spiro-OMeTAD has been used, without exception, as the hole transport material in the research reported here. A precursor solution was prepared inside an Ar-filled glovebox, by subsequent addition of Spiro-OMeTAD (50 mg), chlorobenzene (CB, 547 μL), 4-*tert*-butylpyridine (TBP, 18.7 μL), LiTFSI (11.3 μL) and FK209 (4.9 μL) into a vial. LiTFSI and FK209 were added in the form of their acetonitrile solutions, where the concentrations are 1.88 M and 0.237 M, respectively In the final solution, the Spiro-OMeTAD concentration was calculated to be 63.1 mM (based on CB volume) and the molar ratio Spiro-OMeTAD : TBP : LiTFSI : FK209 is 1 : 0.17 : 0.52 : 0.028. Usually, the Spiro-OMeTAD solution was prepared together with the perovskite precursor solution and also kept sealed, but outside of the glovebox, between preparation and usage.

Deposition of the Spiro-OMeTAD layer was performed after deposition and annealing of the perovskite layer. The samples did not leave the glovebox in between and it was made sure that they had cooled down back to room temperature before addition of the Spiro-OMeTAD layer. To

deposit the Spiro-OMeTAD layer, 40 µL of the precursor solution was dynamically spin coated onto the substrate, where the rotation speed was again 4000 rpm and the spinning time was at least 21 s. After deposition of the Spiro-OMeTAD layer, the samples were taken out of the glovebox and quickly transferred to an inert N_2 atmosphere, where they were kept in the dark.

Au deposition

The final step in the fabrication method of the PSCs was the evaporation of the Au back contact. Prior to the evaporation, the perovskite and Spiro-OMeTAD layers are removed from the area that was previously covered by kapton tape, using a cotton bud and 2-methoxy-ethanol. Also, the cells were broken once more to yield 2.4 cm x 1.4 cm devices (Fig. 4.1d) that fit the mask used for patterning of the Au electrode (see Fig. 4.2). Evaporation was performed using a Leica EM MED020 high vacuum coating system, operating at 7.7×10^{-3}-8.0×10^{-3} mbar, pressures that were typically reached after 1 h of pumping. During the evaporation, the film thickness was monitored using a Leica EM QSG100 quartz crystal film thickness monitor. Evaporation rate was not constant throughout the process, with rate increasing a high thickness (Table 4.1). In total, 80 nm of Au was evaporated in the time frame of ca. 1 h, after which the system was left to cool down for 20-30 min before venting. Again, devices were stored in inert atmosphere in the dark, prior to and in between measurements that would follow.

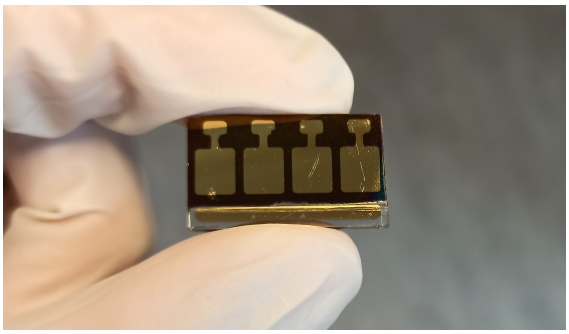

Figure 4.2: Photo of a fully functional perovskite solar cell, showing the pattern created by the gold evaporation mask.

Thickness (nm)	Evaporation rate (nm/s)
0 – 5	< 0.01
5 – 10	0.01
10 – 20	0.02
20 – 80	0.05

Table 4.1: Evaporation rate details for the gold deposition process.

4.3 Characterization

Solar cell performance

The performance of fabricated solar cells was tested by measurement of J-V curves under simulated sunlight. A Wavelabs Sinus-70 LED Solar Simulator (class AAA) was used to reproduce the AM1.5G solar spectrum. J-V curves were obtained via a home-made labVIEW routine and parameter extraction was done via user-defined python scripts. Unless mentioned otherwise, J-V curves were recorded using a light intensity of 100 mW/cm^2 (= 1 sun), a scan rate of 50 mV/s and a step size of 5 mV. Cells were repeatedly scanned in the reverse direction, from 1.2 V to −0.1 V, until a stable (or maximal) PCE was obtained. Only then, a scan in the forward direction was recorded. The active cell area was 0.125 cm^2, which was obtained by covering the devices with a mask containing a circular hole with a diameter of 4 mm.

X-ray photoelectron spectroscopy

X-ray spectroscopy measurements were performed on a PHI Quantera II (Physical Electrons) system. For the recording of the survey spectra, a 200 µm spot size was used, together with 50 W gun power and an operating voltage of 15 kV. The pass filter energy was set to 224 eV and the

acquisition time was set to 100 ms per data point. A step size of 0.1 eV was used. For measurement of the core spectra, the spot size (100 μm), gun power (25 W) and pass energy (55 eV) were lowered. Fitting of the core spectral data was performed with gaussian profiles and a linear background.

Kelvin probe microscopy

Relative work function measurements were performed using a RHC020 Kelvin Probe System (KPTechology). For each sample, the contact potential difference (CPD) was measured on 100 points in an area of 159 μm x 254 μm. The work function of the tip was referenced using an average of 625 CPD measurements of an Au surface, the work function of which was assumed to be 5100 meV. All measurements were performed in relative humidities of less than 9 %.

X-ray diffraction

XRD patterns were obtained using a Siemens D5000 X-ray diffractometer and Cu Kα radiation (λ = 1.54 Å), operating at 45 kV and 40 mA. The spectrum was measured from 2θ = 5.0° up to 60° in steps of 0.05° and a settling time of 3 s. A reference spectrum is created as a 50/50 mix of a measured SnO_2 diffractogram and a diffractogram calculated by Mercury software [39], based on crystallographic data from ref. [40].

Photoluminscence

Photoluminescence (PL) emission spectroscopy measurements were performed using a Fluorolog-3 instrument (FL3-222, Horiba Scientific). The excitation wavelength was 460 nm, whereas the emission spectrum was obtained in the range 700-820 nm, using steps of 1 nm and an acquisition time of 1 s. Both excitation and emission beam slits were set to 5 nm. Samples for PL measurements were fabricated on glass substrates and are illuminated from the glass side, during the experiment.

Scanning electron microscopy

Scanning electron microscopy (SEM) imaging was performed on a Zeiss LEO 1550 FE-SEM. Samples were attached to a carbon support and grounded using silver tape.

Cyclic voltammetry

Cyclic voltammetry experiments were performed using an IviumState.XRe electrochemical interface. A nonaqueous Ag/AgCl (1.0 M in EtOH) reference electrode was used in combination with a carbon counter electrode. For thin film measurements, the FTO slides acted as the working electrode, whereas a Au electrode was used otherwise. The supporting electrolyte solution was 0.1 M NBu_4PF_6 in DMF. Scans were recorded starting from 0 V and from there going to negative voltages. Unless mentioned otherwise, the scan rate was 50 mV/s and the settle time was 100 ms.

Fourier-transform infrared spectroscopy

Fourier-transform infrared spectroscopy experiments were conducted on a VERTEX 70v FT-IR spectrometer (Bruker). The setup was used in absorption mode and acquired data is averaged over 32 individual scans.

DFT calculations

The electronic structure of PA was calculated using DFT calculations as incorporated in the ADF software (v. r79622) [41]. A GGA PBE0 functional and TZ2P basis set were used to describe the electron-electron interactions and atomic orbitals. The choice for the functional was made based on the benchmark study presented in [42]. Before calculation of the dipole moment, the structure was optimized.

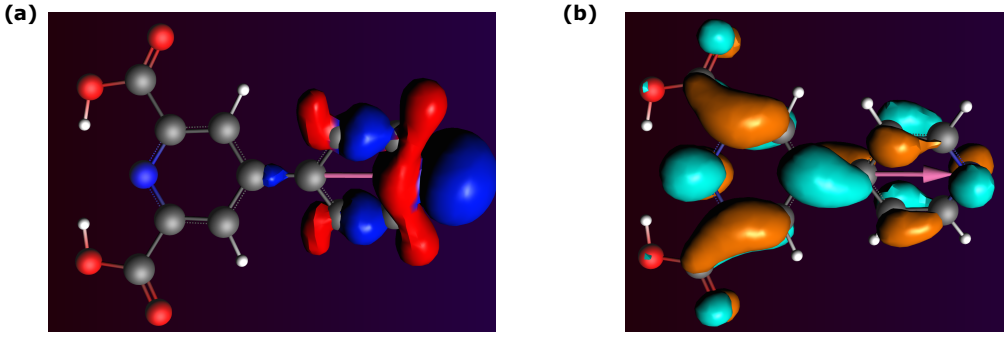

Figure 4.3: HOMO (a) and LUMO (b) molecular orbitals as calculated by DFT. The pink arrow points in the direction of the dipole moment.

5 Results and Discussion

5.1 PA surface modification

XPS

The surface of SnO_2 was modified with PA by immersing the substrates in a PA solution overnight. To confirm the presence of PA, XPS measurements were performed, the results of which are shown in Fig. 5.1. The XPS spectrum of SnO_2, which in its pristine form does not contain any nitrogen atoms, is expected to show a N1s peak upon introduction of PA. In the N1s core spectrum (Fig. 5.1a), a small peak centered at 400.1 eV can indeed be observed. Additionally, carbon atoms in carbonyl groups should result in a C1s peak at 288.0 eV [38]. The C1s spectrum exhibits three peaks, as revealed by gaussian fitting of the data, which are centred around binding energies of 285.2 eV, 286.2 eV and 289.5 eV. Although the two peak at lower binding energies could correspond to C-C/C-H and C-N carbon atoms, respectively, the origin of the peak at 289.5 eV is unknown [14]. Most importantly, the carbonyl carbon peak cannot be observed, suggesting that the surface modification with PA was unsuccessful.

In addition to N1s and C1s spectra, also the Sn3d and O1s core spectra can be used to investigate any changes to the surface of SnO_2 [9, 37]. Upon coverage of the SnO_2 surface, a decrease in peak intensity occurs, while any interaction between Sn and the surface species results in a shift in the binding energy. Although these spectra are obtained for the modified SnO_2 surface, a reference sample was not measured and is therefore not included in the analysis, but the spectra can be found in Fig. A.1.

KPM

In addition to the XPS measurements, KPM measurements were performed to determine the work function of the different SnO_2 layers. A change in the work function is to be expected upon modification of the SnO_2 surface with PA, as a result of the dipole moment of PA [43, 44]. The origin of this change can be understood form the schematic shown in Fig. 5.2. The dipole moment present in PA result in an electric field inside the molecule, between the SnO_2 layer and the layer on top of the SAM. This electric field changes the energy levels of the layers on both sides of PA with respect to each other, where the sign of the change (positive/negative) depends on the orientation of the molecule's dipole moment (see Fig. 5.2). In the case of PA, the dipole moment μ is directed away from the SnO_2 surface, resulting in an electric field directed towards this surface, which in turn lowers the the vacuum level outside the SnO_2.

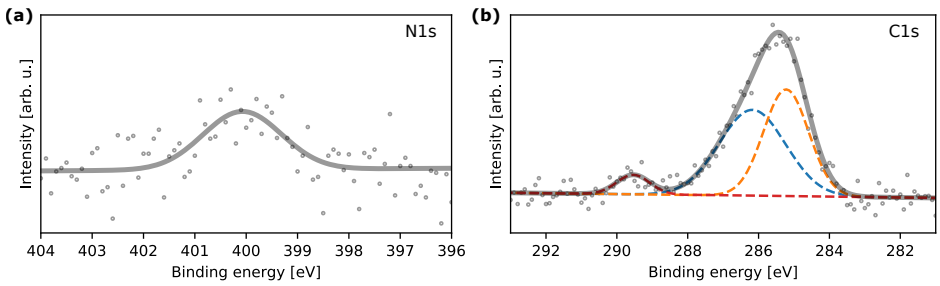

Figure 5.1: N1s (a) and C1s (b) XPS core spectra acquired on PA treated SnO_2 substrates.

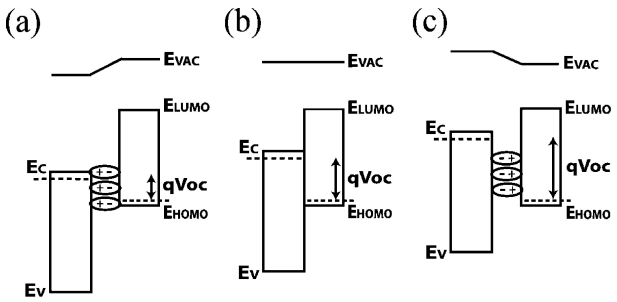

Figure 5.2: Change in work function as a result of surface modification by molecules with a permanent dipole moment. Situation is depicted for a dipole directed towards the surface (a), a dipole moment of zero (b) and a dipole directed away from the surface (c). Adapted from [44].

KPM measurements of PA modified SnO_2 showed a decrease of 0.17 eV in the work function: $\Phi = 3.80$ eV for the PA sample, compared to $\Phi = 3.97$ eV for pristine SnO_2. As a control measurement, a sample was prepared in identical fashion to the PA sample using a blank MeOH solution. The work function of this sample actually increased, compared to that of pristine SnO_2. The KPM results show that the surface of SnO_2 was successfully modified with PA and that its effect on the work function is as expected.

Using density functional theory simulations, the dipole moment of PA was determined to be -1.58 D, where the minus sign denotes that the dipole is directed away from the SnO_2 surface. In comparison to other dipole-induced work function shifts [9, 12], the observed decrease of 0.17 eV is quite big for the moderate dipole moment of PA. For example, a shift of 0.13 eV was observed after introduction of a molecule with a dipole moment of -5.13 D [12].

Solar cell performance

Perovskite solar cells were fabricated by subsequent deposition of $MAPbI_3$, Spiro-OMeTAD and Au layers, on top of the (PA functionalized) SnO_2. Results of the performance tests employed on these cells are shown below, where J-V curves of the champion devices are shown in Fig. 5.3, together with average values collected from multiple cells in Table 5.1. It seems as if the champion devices give a representative view of the averages values, with the treated cells exhibiting slightly worse performance parameters than the pristine SnO_2 samples. There is no specific parameter that shows to be affected greatly by the PA treatment, neither beneficial nor detrimental. In fact, the differences are so small that it is questionable whether any significant change is induced by the treatment procedure. Also the MeOH reference exhibits performance similar to that of SnO_2, with characterization parameters that are slightly worse. It should be noted that only 4 MeOH control cells are included here, compared to more than 20 for SnO_2 and PA cells.

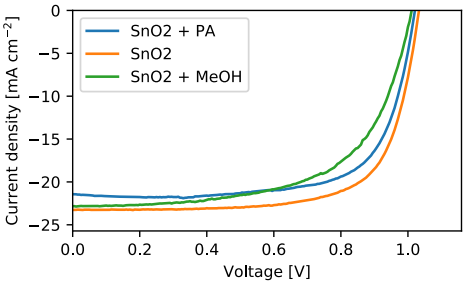

Figure 5.3: J – V curves of champion devices for PA treated, MeOH treated and control SnO_2 cells.

	J_{sc} (mA cm^{-2})	V_{oc} (V)	FF (%)	PCE (%)
SnO_2 + PA	−21.8	0.99	62.6	13.5
SnO_2	−22.0	0.99	62.3	13.6
SnO_2 + MeOH	−21.6	1.0	60.2	13.1

Table 5.1: Averaged solar cell performance parameters for the different types of cells.

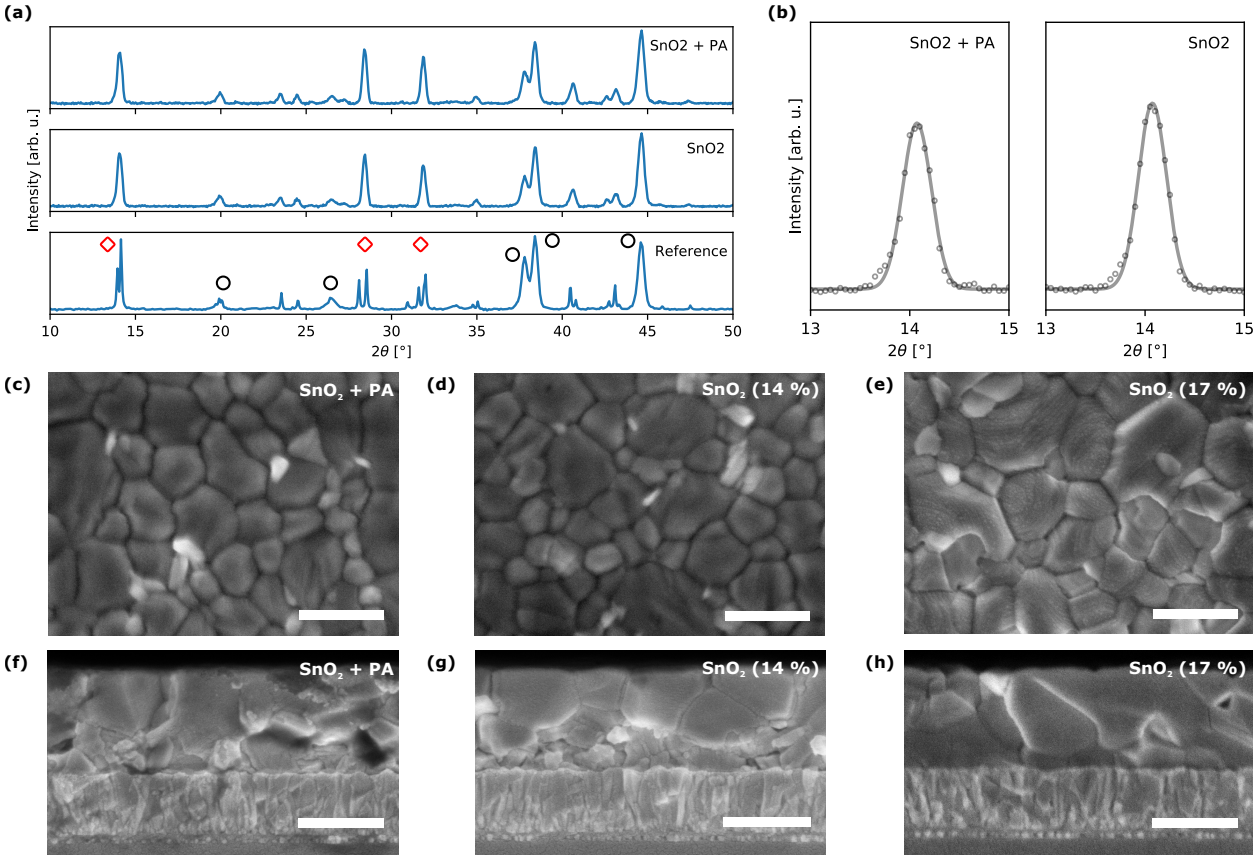

Figure 5.4: (a) XRD pattern of perovskite samples on PA treated and pristine SnO_2, together with a reference spectrum. Some peak have been denoted, where red diamonds correspond to $MAPbI_3$ peak and black circles to SnO_2 peaks. (b) Zoom of the (110)/(200) peak of perovskite, showing to be similar for both treated and control samples. (c-e) Planar SEM images of perovskite layers on PA treated and pristine SnO_2, together with a perovskite layer with a higher PCE. (f-h) Cross-sectional SEM images of the samples of (c-e). Scale bar corresponds to 500 nm in all SEM images.

Further investigation

To further investigate any differences that the inclusion of PA might induce in the perovskite material, more characterization was performed. To this end, X-ray diffraction (XRD) spectra and scanning electron microscopy (SEM) images of FTO / SnO_2 (/PA) / PSK samples were obtained. In the XRD spectra, which are shown in Fig. 5.4, the characteristic peak for $MAPbI_3$ and SnO_2 can be observed. The presence of any PbI_2 can be ruled out, based on the absence of the reflection peak corresponding to its (001) plane at $2\theta = 12.5°$ [45]. The two measured spectra are very similar, not only by eye, but also quantitatively as determined via gaussian fitting of the combined (110)/(200) peak at $2\theta = 14.1°$: the full width half maxima (FWHMs) are nearly identical for samples with (0.341°) and without PA (0.335°), indicating that no significant changes in grain size are induced by the PA treatment. This is in agreement with planar SEM images of the perovskite films, shown in Fig. 5.4c/d, from which no significant changes in grain size or morphology can be observed.

Also cross-sectional SEM images were recorded, which show the same similarity between the two different samples. Interestingly, two different domains inside the perovskite layer can be observed, where the lower one (in contact with SnO_2) consist of grain that are significantly smaller than those in the upper part. This unordered layer can be expected to introduce non-radiative recombination sites, which might be the reason for the observed (average) efficiency of about 14 %. Shown in Fig. 5.4h is a cross-sectional image of a $MAPbI_3$ solar cell from a batch showing PCEs of 17 % fabricated via the same method as the SnO_2 reference cells of Fig. 5.4g. The perovskite layer in

Fig. 5.4h consist of larger grains that are homogeneous throughout the thickness of the layer, which was ca. 500-550 nm for both the low and high efficiency cells. Also from the planar images, the larger grain size can be observed for the higher efficiency cells (see Fig. 5.4e).

PL

To gain more information on the optoelectronic properties of perovskite layers grown on top of PA-SnO_2, steady-state photoluminescence (PL) spectra of the $MAPbI_3$ layers were measured. In contrast to what was observed in previous measurements, there is a big change between the PA sample and the control sample: the PL intensity is reduced by about 50 % upon introduction of the PA interlayer. A tentative explanation for this reduction would be the improved transfer of excited electrons from $MAPbI_3$ to SnO_2, since only radiative recombination inside the perovskite layer will contribute to the PL intensity. In principle however, PL measurements conducted at open-circuit conditions do not allow for probing of charge carrier extraction, because of the requirement for the net current to be equal to zero [46]. Additionally, the decrease in PL intensity can also be a result of an increased amount of non-radiative recombination sites, either inside the bulk of the perovskite layer, or at (one of) its interfaces. This would however be in disagreement with the XRD pattern similarity mentioned above. From this experiment alone, it is not possible to conclude via which mechanism the PL is quenched. Measuring control samples of perovskite layers grown on an insulating substrate, both with and without PA, might shed light on the effect of non-radiative recombination on the PL intensity. In addition, steady-state PL measurements at different excitation intensities and/or time-resolved PL measurements can be performed with the same intention [46]. Alternatively, the trap density could be quantified by space charge limited current measurements using symmetric cells [47].

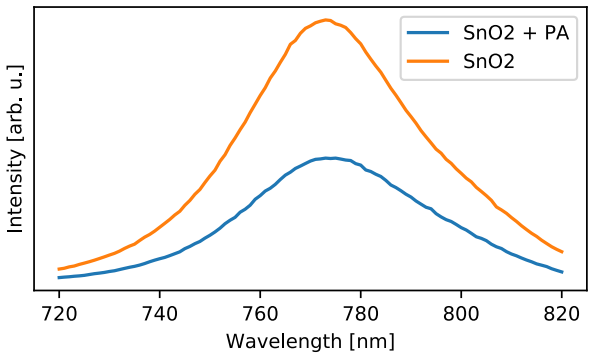

Figure 5.5: Photoluminescence spectra of $MAPbI_3$ grown on top of PA treated and pristine SnO_2.

5.2 NDI as selective contact

To functionalize the surface of FTO with the NDI molecule, a similar method to the PA modification was to used. FTO slides were immersed in a DMF solution of NDI overnight, after which they were rinsed with DMF. Also here, the first thing to do, is to verify whether the surface modification was successful. Therefore, FT-IR absorption spectra of (un)modified FTO substrates were recorded, where specific attention was paid to the range between 1500 cm^{-1} and 2000 cm^{-1}. In the presence of NDI, a peak is expected to be observed here, as a result of the carbonyl functionalities in the molecule. In Fig. 5.6a, the FT-IR absorption spectrum obtained from NDI treated FTO glass is shown. After subtraction of the clean FTO reference absorption, no peaks can be observed, which could mean that the NDI treatment of the FTO slides did not result in the functionalization of its surface. Alternatively, it might be that the signal of the NDI monolayer is too weak to be observed.

Following the example of Johnson et al., the presence of a NDI monolayer was probed via cyclic voltammetry (CV) [38]. In its CV spectrum, NDI shows two peaks at negative voltage, corresponding to the sequential one electron reductions $NDI^0 \longrightarrow NDI^{\bullet -}$ and $NDI^{\bullet -} \longrightarrow NDI^{2-}$, The corresponding redox potentials are $E_{1/2} = -0.96\,V$ and $E_{1/2} = -1.36\,V$ (vs $Fc^{+/0}$). In the CV scans of our FTO treated NDI films, the characteristic NDI peaks cannot be observed, because of the presence of another peak with a larger magnitude. This peak was demonstrated to originate from (impurities in) the electrolyte solution, by measuring the CV scan of the blank electrolyte solution (see Fig. 5.6b). The square root dependence of the peak height on the scan rate confirms the idea of impurities inside the electrolyte (Fig. 5.6c, d) [48].

To be able to measure the presence of NDI via CV, these impurities should be removed from the electrolyte. Purification of the electrolyte (NBu_4PF_6) can be done by crystallisation from ethanol, for example. Optionally, the outcome of the experiment might be improved by conduction in an inert atmosphere, such as N_2. We however chose not to do this and turned to other characterization techniques to determine whether NDI was successfully adsorbed onto the FTO surface.

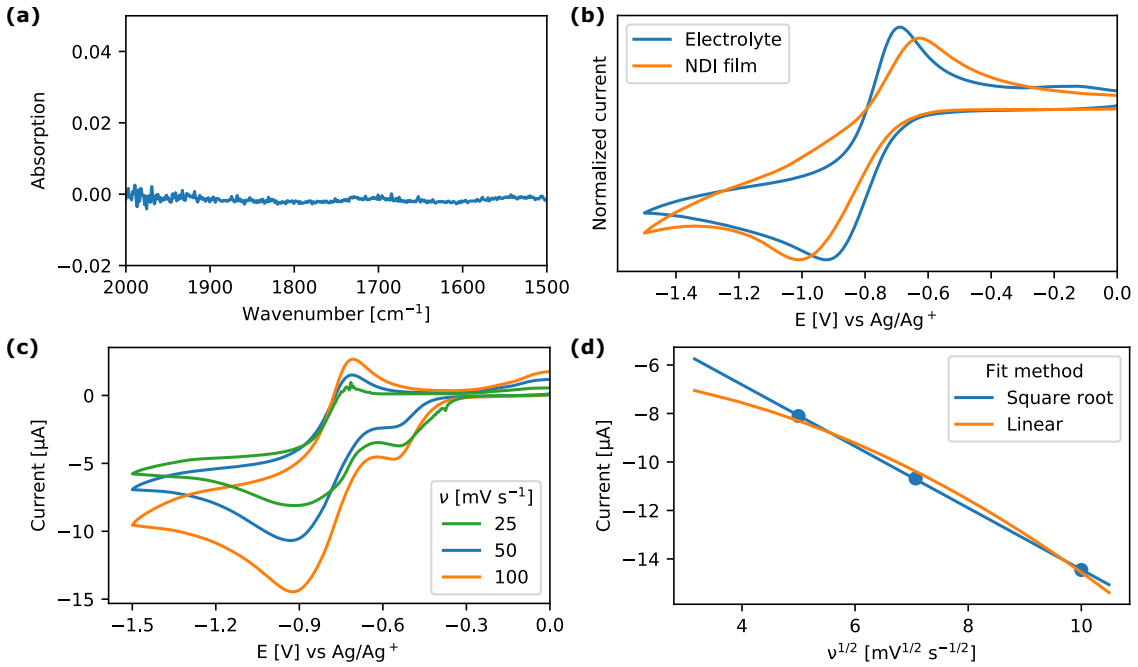

Figure 5.6: (a) FT-IR absorption spectra of NDI treated FTO substrate, corrected for absorption by the FTO. (b) CV scans of a NDI treated FTO substrate and the blank electrolyte solution. (c) CV scans of the blank electrolyte solution at different scan rates ν. (d) Dependence of peak current on scan rate, exhibiting a square-root dependence.

XPS

For the investigation of the FTO surface by XPS, we particularly focused on the N1s and C1s core spectra, since in the ideal case the only nitrogen and carbon containing species would be the NDI molecule. In the N1s spectrum, two peaks can be observed that are centred around 400.7 eV and 407.3 eV. The intensity of the peaks is rather weak, as can be expected for a monolayer. The position of the lower binding energy peak corresponds well to reported values for napthalene diimide derivatives [38, 49]. The origin of the peak at a binding energy 407.3 eV is unknown, but its position suggest a highly oxidized nitrogen functionality, for example in the form of a nitro group ($-NO_2$) [50].

Analysis of the C1s spectrum reveals the presence of three peak at binding energies of 285.1 eV, 288.4 eV and 293.1 eV. The lowest energy peak can be attributed to the presence of aliphatic carbon atoms, whereas the peaks at higher binding energies could correspond to carbon atoms in a carbonyl functionality (288.4 eV) and an aromatic system (293.1 eV) [49]. Based on the presence of the two latter peaks, it seems as if NDI is present on the surface of FTO, a thought that is supported by the N1s spectrum. The presence of NDI should however also result in a C-N peak in the C1s spectrum, but this is not what is observed. Although the proof is not definite, we did think the NDI deposition was successful, mostly because of the N1s peak. As for the XPS analysis devoted to the PA molecule, more information might be obtained through the Sn3d and O1s core spectra, given that a suitable control sample is also measured. Since we did not do so, these spectra are not covered here, but are shown in Fig. B.2.

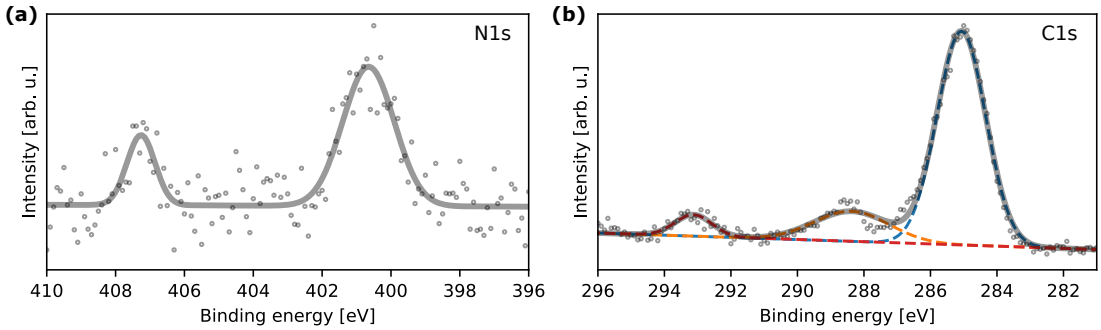

Figure 5.7: N1s (a) and C1s (b) XPS core spectra of NDI treated FTO substrates.

KPM

To further confirm the presence of NDI, the work function of the functionalized FTO substrates was measured using KPM. In this way, the work function of NDI treated FTO substrates (4.33 ± 0.01 eV) was found to be equal to that of UV-ozone treated FTO (4.33 ± 0.02 eV). Interestingly, the work function of a sample that was heated to 60 °C during the NDI deposition, was found to be 4.08 ± 0.01 eV, corresponding to a decrease of 0.25 eV. From this, it seems as if the deposition of the NDI molecule only occurs at slightly elevated temperature. Note that this disagrees with the results from XPS, from which the deposition seemed to be successful already at room temperature. Combined effects from solvent and heat form an alternative explanation for the observed decrease in the work function. To rule out or confirm this, control samples with the blank solvent should be measured.

As a matter of fact, it is unknown to us what expect from the influence of NDI on the work function of FTO. Although self-assembled monolayers have shown to affect the work function of metal oxides [14], the molecules employed in these examples possess a dipole moment in addition to their redox activity. Whether any changes in the work function will be connected to the redox activity, rather solely being a dipole induced effect, cannot be said. The absence of a dipole moment in the NDI molecule, which follows from symmetry considerations, means that its effect on the work function is yet to be revealed.

Solar cell performance

From the surface and thin-film characterization techniques, we have not been able to determine whether NDI was successfully attached to the FTO surface. If however, the NDI molecule turns out to be an effective selective contact, cells with NDI should show different solar cell performance behaviour compared to the ETL-free control devices. Thus, solar cell devices have been fabricated by sequential deposition of $MAPbI_3$, Spiro-OMeTAD and Au layers and their performance was tested via the measurement of J-V curves under simulated sunlight. The results of this are shown both graphically (Fig. 5.8a) via the J-V curves of the champion devices, as well as numerically (Table 5.2) via the averaged performance parameters.

NDI cells show worsened power conversion efficiency compared to FTO cells, which seems to be a result of a decreased short-circuit current J_{sc}. The open-circuit V_{oc} and FF on the other hand, seem not to be affected by the NDI treatment. From this, it seems as if the presence of the NDI monolayer does not lead to any increase in electron selectivity, which is expected to lead to an increase of both V_{oc} and FF. The other, obvious alternative explanation for the observed results is the absence of the NDI monolayer between the FTO electrode and the absorber layer.

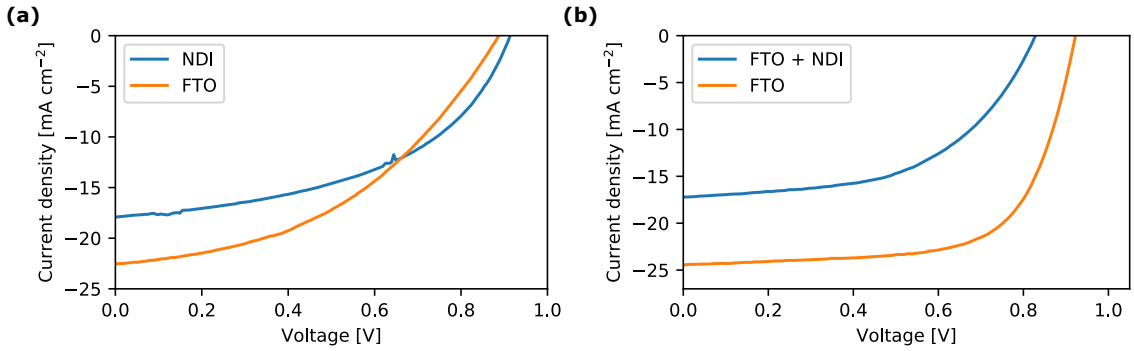

Figure 5.8: J – V curves of champion devices, of both NDI treated FTO substrates and pristine FTO. (a) $MAPbI_3$, treatment at room temperature. (b) $(Cs, FA, MA)Pb(I, Br, Cl)_3$, treatment at 60 °C.

	J_{sc} (mA cm^{-2})	V_{oc} (V)	FF (%)	PCE (%)
FTO + NDI	−16.5	0.91	42.3	6.4
FTO	−18.0	0.90	42.6	7.0

Table 5.2: Averaged solar cell performance parameters for the different types of $MAPbI_3$ cells.

In addition to the $MAPbI_3$-based perovskite solar cells, devices using a triple cation, triple anion $(Cs, FA, MA)Pb(I, Br, Cl)_3$ perovskite were fabricated to investigate the selectivity behaviour of the NDI monolayer. This mixed perovskite is known to enable the fabrication of PSCs with efficiencies exceeding 20 % and more importantly, it shows high reproducibility. Devices with and without the NDI layer were fabricated and the obtained J-V curves of these solar cells are shown in Fig. 5.8b. Here, the difference between the two types of cells is more evident, with decreases in all performance parameters.

From the characterization data shown above, it is concluded that the NDI functionalization negatively affects the growth of the perovskite layer. Although from the J-V data it seems as if there is no ETL, this does not give any insight into whether the deposition of NDI was successful. The absence of an ETL can namely not only be explained by the absence of NDI, since it could also be that NDI is not able to act as a good ETL. In case of the latter, it would be interesting to be able to explain this, since monolayer selective contacts have shown to be able to work properly [13, 14] and the NDI redox potential seems to be suitable for alignment with perovskite energy levels. Again, it might be that the absence of a permanent dipole moment makes the NDI molecule inherently different from the molecules already employed in monolayer selective contacts.

	J_{sc} (mA cm^{-2})	V_{oc} (V)	FF (%)	PCE (%)
SnO_2 + NDI	−20.3	0.95	53.3	10.3
SnO_2	−22.1	0.98	57.4	12.5

Table 5.3: Averaged solar cell performance parameters for the different types of $MAPbI_3$ cells.

5.3 NDI surface modification

In addition to the use of NDI as a selective contact, its possibilities to function as a SnO_2 passivation layer was also investigated. The effect of the surface modification (procedure) on the SnO_2 layer was investigated by measuring its work function. It was found that the work function of SnO_2 (3.97 ± 0.02 eV) was increased with 0.23 eV to 4.20 ± 0.07 eV after immersion of the substrates in a NDI/DMF solution overnight. The work function also increased by 0.33 eV to 4.30 ± 0.08 eV when the substrate was exposed to a blank DMF solution, for the same amount of time. These results, in combination with the monolayer analysis results covered above for the SnO_2/PA and FTO/NDI, do not allow us to decide whether the monolayer deposition was successful. Solar cells were fabricated nevertheless and the results of their characterization is shown below.

Solar cell performance

From the J-V characteristics obtained for $MAPbI_3$-based PSCs, shown inFig. 5.9a, it can be seen that the NDI treatment at room temperature has a negative effect on the solar cell performance. The efficiencies of the NDI treated samples is about 2 % lower than that of the cell employing the pristine SnO_2 ETL, where the biggest change seems to come from the decreased short-circuit current although both V_{oc} and FF also decreased slightly. In case of the mixed perovskite, the NDI treatment was performed at 60 °C. Now, the difference between the solar cell performance of NDI and control cells was much bigger (Fig. 5.9). The passivation treatment has led to a major decrease in solar cell efficiency, suggesting that the perovskite layer growth is severely affected by the NDI treatment. It could also be that the NDI deposition method has a detrimental effect on the quality of the SnO_2 layer and that this is the reason for the drop in efficiency. Fabrication of control samples where the SnO_2 substrates undergo the same deposition method with a blank DMF solution might shed light on the origin of the poor performance.

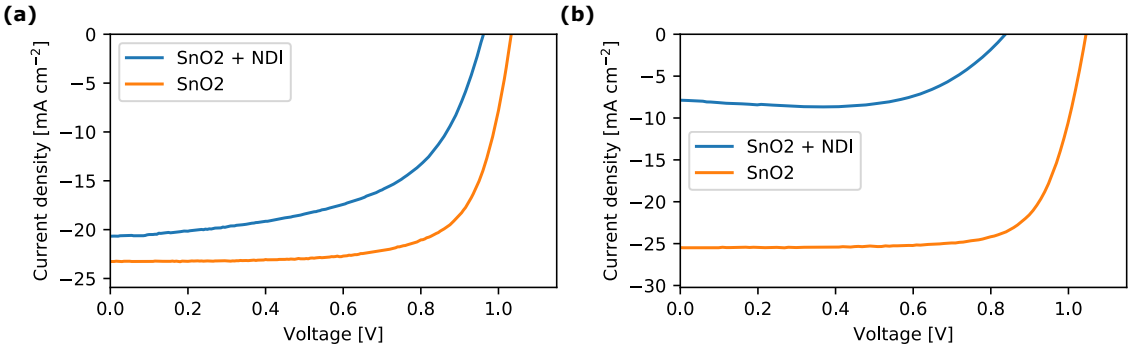

Figure 5.9: Champion J − V curves of NDI treated SnO_2 samples, together with control samples. (a) $MAPbI_3$, treatment at room temperature. (b) (Cs, FA, MA)Pb(I, Br, Cl)$_3$, treatment at 60 °C.

6 Conclusions

Functionalization of the surface of SnO_2 selective contacts with PA was performed using a bath deposition method. The presence of PA was assumed after observation of a decrease in the work function of the layer after modification, as measured using KPM. XPS measurements were not able to support the results from the KPM measurements. Perovskite solar cells were fabricated using the FTO / SnO_2 / $MAPbI_3$ / Spiro-OMeTAD / Au structure, where both pristine and PA treated SnO_2 was used. PA treated cells exhibited lower efficiencies, but the differences were found to be minimal. The observed similarity in device performance is unexpected, based on the decreased work function and reported accompanied effects [9, 12]. Characterization by XRD and SEM revealed the perovskite layer not to be significantly changed in the presence of PA. Steady state PL intensity on the other, was found to be significantly reduced, which could be related to improved charge extraction.

The surface of FTO was treated with an NDI solution and the presence of NDI was afterwards checked by means of XPS and KPM. From the XPS measurements, the NDI molecule appears to be present after bath deposition at room temperature, but a change in the work function was only observed when the procedure was performed at 60 °C. Additionally, CV and FT-IR were used in unsuccessful attempts to indicate the presence of NDI. The presence of NDI could therefore not be verified. Devices using NDI treated FTO substrates exhibited lower PCE values, both using $MAPbI_3$ and $(Cs, FA, MA)Pb(I, Br, Cl)_3$ as the absorber layer. From the J-V curves, it was concluded that the NDI treatment procedure negatively affects perovskite layer growth and therefore, the device performance. It cannot be determined whether the observed differences are actually due to the presence of the NDI monolayer or a result of the modification procedure.

NDI modification of the SnO_2 ETL was also performed, where again the presence of the molecular monolayer could not be determined. The influence of the modification procedure on the solar cell performance was found to be negative, but also here, the reason for this could not be elucidated.

7 Outlook

Interpretation of the results obtained in the research reported here was mostly limited by ambiguities concerning the presence or absence of molecular monolayers. The reason for this is rather obvious: the amount of material inside this monolayer is so little that only little signal can be obtained using essentially any characterization techniques. More information might be obtained using the same techniques used here (XPS, KPM) using more accurate characterization parameters, e.g. longer collection times, and inclusion of appropriate control samples prepared in parallel. In addition, other surface sensitive characterization techniques could be used, such as contact angle measurements.

Another suggestion for future research would be to use a perovskite material that shows a higher reproducibility. The spread in measured efficiencies using $MAPbI_3$ cells is rather larger, making it hard to tell apart declines or improvements from statistical variations. The mixed $(Cs, FA, MA)Pb(I, Br, Cl)_3$ perovskite material could be a candidate for this. A possible downside of the use of mixed perovskite materials is the increased complexity induced by the composition of the perovskite material.

Once a set of characterization methods has been found that allows for reliable determination of monolayer presence, the effects of the monolayers can be explored. One has a high degree of control concerning the properties of the molecules, which allows one to systematically vary parameters. In this way, the fundamental understanding of perovskite materials and solar cells can be improved and possibly, solar cells with high stability and efficiency can be fabricated. Additionally, the facile method of deposition (bath deposition) suggests that monolayer selective contacts and/or interlayer are relatively easily applied to large scale fabrication processes.

Acknowledgements

During this internship, I have learned a lot of new things, new ways of thinking, new ways of problem solving. Although I will be out of the field of photovoltaics for the coming years, I might return to as it did not disappoint me. Therefore, I would like to thank *Gerrit*, for making it possible for me to do this project. Additionally, I would like to thank you, together with *Kim*, for the discussions and general supervision. Then I would like to acknowledge *Petra de Jongh* for taking up the role of the second supervisor. Lastly, thank you *Jos Mulkens* for performing the DFT calculations, even in more details than requested.

Only five months ago, I had no idea what to expect from this semester abroad. A lot of research, of course, but in a totally new field, in a new country with a lot of new people. Luckily, in the end, everything turned out to be fine. The research? Incredibly interesting, but also incredibly difficult. The country? Perfect, arguably the best place to be during a pandemic. And how about the people? Well, the people turned out to be the best of it all. Although I am of course thankful to everyone in the group for the nice time I have had, I would especially like to thank *Hannes*, *Aneta* and *Rima*, but also *Rex*, *Masoud* and *Sepideh*. Without you guys, my stay in Sweden would have been a lot more lonely and a lot less fun. That we may meet again in the near future, cheers!

References

[1] Reinders, A.; Verlinden, P.; van Sark, W.; Freundlich, A. *Photovoltaic Solar Energy: from fundametals to applications*, 1st ed.; John Wiley & Sons, Ltd, 2017.

[2] Lindsey, R. If carbon dioxide hits a new high every year, why isn't every year hotter than the last? https://www.climate.gov/news-features/climate-qa/if-carbon-dioxide-hits-new-high-every-year-why-isn't-every-year-hotter-last.

[3] IEA, Solar PV power generation in the Sustainable Development Scenario, 2000-2030. https://www.iea.org/data-and-statistics/charts/solar-pv-power-generation-in-the-sustainable-development-scenario-2000-2030.

[4] NREL, Best Research-Cell Efficiency Chart. https://www.nrel.gov/pv/assets/pdfs/best-research-cell-efficiencies.20200406.pdf.

[5] Kojima, A.; Teshima, K.; Shirai, Y.; Miyasaka, T. Organometal Halide Perovskites as Visible-Light Sensitizers for Photovoltaic Cells. *Journal of the American Chemical Society* **2009**, *131*, 6050–6051, DOI: 10.1021/ja809598r.

[6] Park, N. Research Direction toward Scalable, Stable, and High Efficiency Perovskite Solar Cells. *Advanced Energy Materials* **2020**, *10*, 1903106, DOI: 10.1002/aenm.201903106.

[7] Jena, A. K.; Kulkarni, A.; Miyasaka, T. Halide Perovskite Photovoltaics: Background, Status, and Future Prospects. *Chemical Reviews* **2019**, *119*, 3036–3103, DOI: 10.1021/acs.chemrev.8b00539.

[8] Chen, Y.; Zhang, L.; Zhang, Y.; Gao, H.; Yan, H. Large-area perovskite solar cells-a review of recent progress and issues. *RSC Advances* **2018**, *8*, 10489–10508, DOI: 10.1039/c8ra00384j.

[9] Choi, K.; Lee, J.; Kim, H. I.; Park, C. W.; Kim, G.-W.; Choi, H.; Park, S.; Park, S. A.; Park, T. Thermally stable, planar hybrid perovskite solar cells with high efficiency. *Energy & Environmental Science* **2018**, *11*, 3238–3247, DOI: 10.1039/C8EE02242A.

[10] Wolff, C. M. et al. Perfluorinated Self-Assembled Monolayers Enhance the Stability and Efficiency of Inverted Perovskite Solar Cells. *ACS Nano* **2020**, *14*, 1445–1456, DOI: 10.1021/acsnano.9b03268.

[11] Tumen-Ulzii, G.; Matsushima, T.; Klotz, D.; Leyden, M. R.; Wang, P.; Qin, C.; Lee, J.-W.; Lee, S.-j.; Yang, Y.; Adachi, C. Hysteresis-less and stable perovskite solar cells with a self-assembled monolayer. *Communications Materials* **2020**, *1*, 31, DOI: 10.1038/s43246-020-0028-z.

[12] Azmi, R.; Hadmojo, W. T.; Sinaga, S.; Lee, C.-L.; Yoon, S. C.; Jung, I. H.; Jang, S.-Y. High-Efficiency Low-Temperature ZnO Based Perovskite Solar Cells Based on Highly Polar, Nonwetting Self-Assembled Molecular Layers. *Advanced Energy Materials* **2018**, *8*, 1701683, DOI: 10.1002/aenm.201701683.

[13] Yalcin, E.; Can, M.; Rodriguez-Seco, C.; Aktas, E.; Pudi, R.; Cambarau, W.; Demic, S.; Palomares, E. Semiconductor self-assembled monolayers as selective contacts for efficient PiN perovskite solar cells. *Energy & Environmental Science* **2019**, *12*, 230–237, DOI: 10.1039/C8EE01831F.

[14] Al-Ashouri, A. et al. Conformal monolayer contacts with lossless interfaces for perovskite single junction and monolithic tandem solar cells. *Energy & Environmental Science* **2019**, *12*, 3356–3369, DOI: 10.1039/C9EE02268F.

[15] Donev, J. Dopant - Energy Education. https://energyeducation.ca/encyclopedia/Dopant.

[16] Smets, A.; Jäger, K.; Olindo, I.; van Swaaij, R.; Zeman, M. *Solar Energy: The Physics and Engineering of Photovoltaic Conversion Technology and Systems*; UTI Cambridge.

[17] Rühle, S. Tabulated values of the Shockley–Queisser limit for single junction solar cells. *Solar Energy* **2016**, *130*, 139–147, DOI: 10.1016/j.solener.2016.02.015.

[18] NREL, Reference Air Mass 1.5 Spectra: ASTM G-173. https://www.nrel.gov/grid/solar-resource/spectra-am1.5.html.

[19] Shockley, W.; Queisser, H. J. Detailed balance limit of efficiency of p-n junction solar cells. *Journal of Applied Physics* **1961**, *32*, 510–519, DOI: 10.1063/1.1736034.

[20] Kim, H.-S.; Lee, C.-R.; Im, J.-H.; Lee, K.-B.; Moehl, T.; Marchioro, A.; Moon, S.-J.; Humphry-Baker, R.; Yum, J.-H.; Moser, J. E.; Grätzel, M.; Park, N.-G. Lead Iodide Perovskite Sensitized All-Solid-State Submicron Thin Film Mesoscopic Solar Cell with Efficiency Exceeding 9%. *Scientific Reports* **2012**, *2*, 591, DOI: 10.1038/srep00591.

[21] Lee, M. M.; Teuscher, J.; Miyasaka, T.; Murakami, T. N.; Snaith, H. J. Efficient Hybrid Solar Cells Based on Meso-Superstructured Organometal Halide Perovskites. *Science* **2012**, *338*, 643–647, DOI: 10.1126/science.1228604.

[22] Green, M. A.; Ho-Baillie, A.; Snaith, H. J. The emergence of perovskite solar cells. *Nature Photonics* **2014**, *8*, 506–514, DOI: 10.1038/nphoton.2014.134.

[23] Yang, T. C.-J.; Fiala, P.; Jeangros, Q.; Ballif, C. High-Bandgap Perovskite Materials for Multijunction Solar Cells. *Joule* **2018**, *2*, 1421–1436, DOI: 10.1016/j.joule.2018.05.008.

[24] Ossila, Perovskites and Perovskite Solar Cells: An Introduction. https://www.ossila.com/pages/perovskites-and-perovskite-solar-cells-an-introduction.

[25] Wikipedia, Methylammonium lead halide. https://en.wikipedia.org/wiki/Methylammonium{_}lead{_}halide.

[26] Yin, W.-J.; Shi, T.; Yan, Y. Superior Photovoltaic Properties of Lead Halide Perovskites: Insights from First-Principles Theory. *The Journal of Physical Chemistry C* **2015**, *119*, 5253–5264, DOI: 10.1021/jp512077m.

[27] Ahn, N.; Son, D.-Y.; Jang, I.-H.; Kang, S. M.; Choi, M.; Park, N.-G. Highly Reproducible Perovskite Solar Cells with Average Efficiency of 18.3% and Best Efficiency of 19.7% Fabricated via Lewis Base Adduct of Lead(II) Iodide. *Journal of the American Chemical Society* **2015**, *137*, 8696–8699, DOI: 10.1021/jacs.5b04930.

[28] Burschka, J.; Pellet, N.; Moon, S.-J.; Humphry-Baker, R.; Gao, P.; Nazeeruddin, M. K.; Grätzel, M. Sequential deposition as a route to high-performance perovskite-sensitized solar cells. *Nature* **2013**, *499*, 316–319, DOI: 10.1038/nature12340.

[29] Im, J.-H.; Kim, H.-S.; Park, N.-G. Morphology-photovoltaic property correlation in perovskite solar cells: One-step versus two-step deposition of CH 3 NH 3 PbI 3. *APL Materials* **2014**, *2*, 081510, DOI: 10.1063/1.4891275.

[30] Eames, C.; Frost, J. M.; Barnes, P. R. F.; O'Regan, B. C.; Walsh, A.; Islam, M. S. Ionic transport in hybrid lead iodide perovskite solar cells. *Nature Communications* **2015**, *6*, 7497, DOI: 10.1038/ncomms8497.

[31] Weber, S. A. L.; Hermes, I. M.; Turren-Cruz, S.-H.; Gort, C.; Bergmann, V. W.; Gilson, L.; Hagfeldt, A.; Graetzel, M.; Tress, W.; Berger, R. How the formation of interfacial charge causes hysteresis in perovskite solar cells. *Energy & Environmental Science* **2018**, *11*, 2404–2413, DOI: 10.1039/C8EE01447G.

[32] Bertoluzzi, L.; Boyd, C. C.; Rolston, N.; Xu, J.; Prasanna, R.; O'Regan, B. C.; McGehee, M. D. Mobile Ion Concentration Measurement and Open-Access Band Diagram Simulation Platform for Halide Perovskite Solar Cells. *Joule* **2020**, *4*, 109–127, DOI: 10.1016/j.joule.2019.10.003.

[33] Jiang, Q.; Zhang, L.; Wang, H.; Yang, X.; Meng, J.; Liu, H.; Yin, Z.; Wu, J.; Zhang, X.; You, J. Enhanced electron extraction using SnO2 for high-efficiency planar-structure HC(NH2)2PbI3-based perovskite solar cells. *Nature Energy* **2017**, *2*, 16177, DOI: 10.1038/nenergy.2016.177.

[34] Correa Baena, J. P.; Steier, L.; Tress, W.; Saliba, M.; Neutzner, S.; Matsui, T.; Giordano, F.; Jacobsson, T. J.; Srimath Kandada, A. R.; Zakeeruddin, S. M.; Petrozza, A.; Abate, A.; Nazeeruddin, M. K.; Grätzel, M.; Hagfeldt, A. Highly efficient planar perovskite solar cells through band alignment engineering. *Energy & Environmental Science* **2015**, *8*, 2928–2934, DOI: 10.1039/C5EE02608C.

[35] Calió, L.; Kazim, S.; Grätzel, M.; Ahmad, S. Hole-Transport Materials for Perovskite Solar Cells. *Angewandte Chemie International Edition* **2016**, *55*, 14522–14545, DOI: 10.1002/anie.201601757.

[36] Singh, R.; Singh, P. K.; Bhattacharya, B.; Rhee, H.-W. Review of current progress in inorganic hole-transport materials for perovskite solar cells. *Applied Materials Today* **2019**, *14*, 175–200, DOI: 10.1016/j.apmt.2018.12.011.

[37] Wang, J.; Datta, K.; Weijtens, C. H. L.; Wienk, M. M.; Janssen, R. A. J. Insights into Fullerene Passivation of SnO 2 Electron Transport Layers in Perovskite Solar Cells. *Advanced Functional Materials* **2019**, *29*, 1905883, DOI: 10.1002/adfm.201905883.

[38] Johnson, B. A.; Bhunia, A.; Fei, H.; Cohen, S. M.; Ott, S. Development of a UiO-Type Thin Film Electrocatalysis Platform with Redox-Active Linkers. *Journal of the American Chemical Society* **2018**, *140*, 2985–2994, DOI: 10.1021/jacs.7b13077.

[39] CCDC, Mercury. http://www.ccdc.cam.ac.uk/mercury/{%}0A.

[40] Yamada, Y.; Yamada, T.; Phuong, L. Q.; Maruyama, N.; Nishimura, H.; Wakamiya, A.; Murata, Y.; Kanemitsu, Y. Dynamic Optical Properties of CH3NH3PbI3 Single Crystals As Revealed by One- and Two-Photon Excited Photoluminescence Measurements. *Journal of the American Chemical Society* **2015**, *137*, 10456–10459, DOI: 10.1021/jacs.5b04503.

[41] te Velde, G.; Bickelhaupt, F. M.; Baerends, E. J.; Fonseca Guerra, C.; van Gisbergen, S. J. A.; Snijders, J. G.; Ziegler, T. Chemistry with ADF. *Journal of Computational Chemistry* **2001**, *22*, 931–967, DOI: 10.1002/jcc.1056.

[42] Hait, D.; Head-Gordon, M. How Accurate Is Density Functional Theory at Predicting Dipole Moments? An Assessment Using a New Database of 200 Benchmark Values. *Journal of Chemical Theory and Computation* **2018**, *14*, 1969–1981, DOI: 10.1021/acs.jctc.7b01252.

[43] Khodabakhsh, S.; Poplavskyy, D.; Heutz, S.; Nelson, J.; Bradley, D. D. C.; Murata, H.; Jones, T. S. Using Self-Assembling Dipole Molecules to Improve Hole Injection in Conjugated Polymers. *Advanced Functional Materials* **2004**, *14*, 1205–1210, DOI: 10.1002/adfm.200400035.

[44] Goh, C.; Scully, S. R.; McGehee, M. D. Effects of molecular interface modification in hybrid organic-inorganic photovoltaic cells. *Journal of Applied Physics* **2007**, *101*, 114503, DOI: 10.1063/1.2737977.

[45] Wang, R. et al. Caffeine Improves the Performance and Thermal Stability of Perovskite Solar Cells. *Joule* **2019**, *3*, 1464–1477, DOI: 10.1016/j.joule.2019.04.005.

[46] Hutter, E. M.; Kirchartz, T.; Ehrler, B.; Cahen, D.; von Hauff, E. Pitfalls and prospects of optical spectroscopy to characterize perovskite-transport layer interfaces. *Applied Physics Letters* **2020**, *116*, 100501, DOI: 10.1063/1.5143121.

[47] Duijnstee, E. A.; Ball, J. M.; Le Corre, V. M.; Koster, L. J. A.; Snaith, H. J.; Lim, J. Toward Understanding Space-Charge Limited Current Measurements on Metal Halide Perovskites. *ACS Energy Letters* **2020**, 376–384, DOI: 10.1021/acsenergylett.9b02720.

[48] Elgrishi, N.; Rountree, K. J.; McCarthy, B. D.; Rountree, E. S.; Eisenhart, T. T.; Dempsey, J. L. A Practical Beginner's Guide to Cyclic Voltammetry. *Journal of Chemical Education* **2018**, *95*, 197–206, DOI: 10.1021/acs.jchemed.7b00361.

[49] Frath, D.; Nguyen, V. Q.; Lafolet, F.; Martin, P.; Lacroix, J.-C. Electrografted monolayer based on a naphthalene diimide–ruthenium terpyridine complex dyad: efficient creation of large-area molecular junctions with high current densities. *Chemical Communications* **2017**, *53*, 10997–11000, DOI: 10.1039/C7CC04972B.

[50] NIST, NIST X-ray Photoelectron Spectroscopy Database. https://srdata.nist.gov/xps/.

Appendices

A. Additional XPS spectra PA

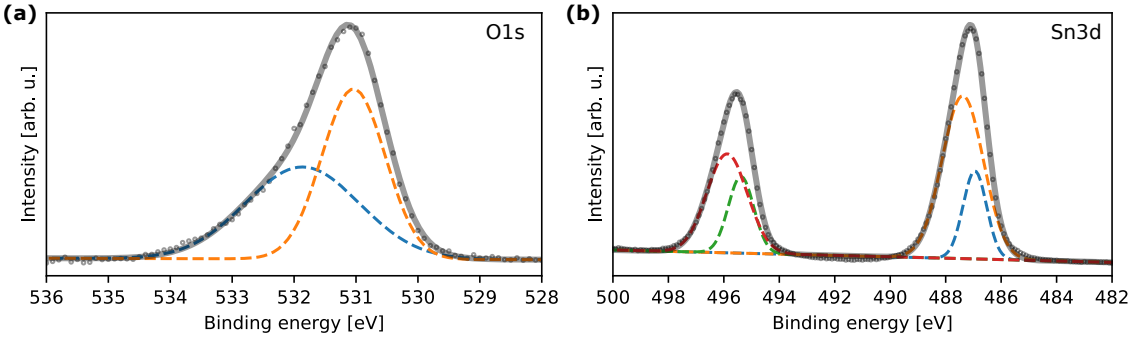

Figure A.1: O1s (a) and Sn3d (b) core XPS spectra measured on PA treated SnO_2 substrates.

B. Additional XPS spectra NDI

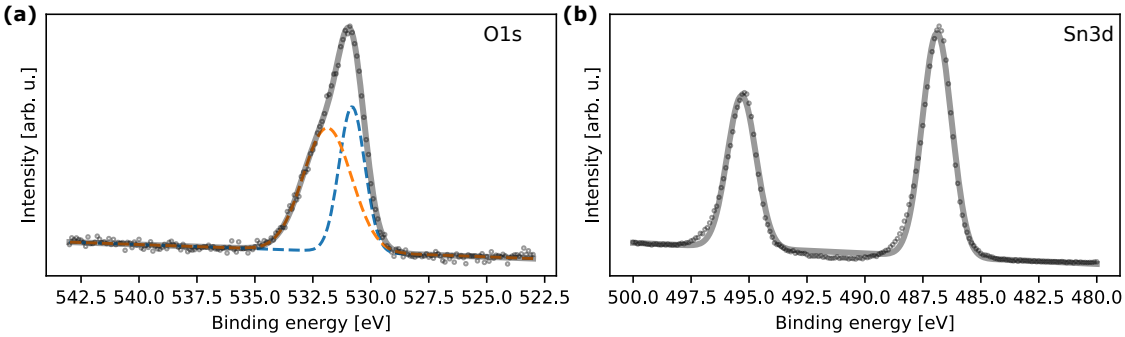

Figure B.2: O1s (a) and Sn3d (b) core XPS spectra measured on NDI treated FTO substrates.